

See discussions, stats, and author profiles for this publication at: <https://www.researchgate.net/publication/243658227>

Counterion surface diffusion in a lyotropic mesophase. A ^{23}Na two-dimensional quadrupolar echo NMR relaxation study

ARTICLE *in* THE JOURNAL OF PHYSICAL CHEMISTRY · MARCH 1990

Impact Factor: 2.78 · DOI: 10.1021/j100369a070

CITATIONS

48

READS

31

4 AUTHORS, INCLUDING:



Istvan Furo

KTH Royal Institute of Technology

168 PUBLICATIONS 2,779 CITATIONS

SEE PROFILE



Per-Ola Quist

AstraZeneca

32 PUBLICATIONS 630 CITATIONS

SEE PROFILE



Tuck C Wong

University of Missouri

108 PUBLICATIONS 1,690 CITATIONS

SEE PROFILE

clusion compound of CDx, 1-propanol, and N), and NC·AC (exciplex) fluorescence by I^- and IO_3^- have been carried out, and the results are tabulated in Table III together with fluorescence lifetimes for these species. As is usually the case, rate constants for fluorescence quenching of NC by I^- and IO_3^- are reduced by about one-fourth and one-seventh relative to those of N, respectively, indicating the protection by CDx from the quenchers. The most plausible structures of NC·NC and NC·AC are such that the two CDx cavities are associated facing each other (a head-to-head, head-to-tail, or tail-to-tail orientation). In this case, I^- must approach and quench the excimer or exciplex inside the connected cavities from the two open ends of the cavities. The same is true for the quenching of NC (N within the cavity), although in this case only one CDx molecule is relevant. Consequently, rate constants for fluorescence quenching of NC, NC·NC (excimer), and NC·AC (exciplex) by I^- are almost identical. For NPrC, on the other hand, I^- can attack an N molecule inside the cavity only from the other uncapped (un-

floored) open end because in NPrC one of the two open ends of the cavity is capped (floored) by 1-propanol. As a result, a quenching rate constant for NPrC is about half those for NC, NC·NC, and NC·AC. Quenching of the excimer, exciplex, and NPrC by IO_3^- is quite different from that by I^- : slight enhancement of the excimer, exciplex, and NPrC emissions by IO_3^- rather than quenching is observed. Similar quenching behavior by IO_3^- has been reported for a 2-methoxynaphthalene-1,2-dicyanobenzene complex (CDx-2-methoxynaphthalene-1,2-dicyanobenzene system).¹⁸ No quenching by IO_3^- is attributed in part to the bulkiness of IO_3^- compared with I^- . However, the negative quenching (intensity enhancement) effect of IO_3^- cannot clearly be explained at present, although there is a possibility that IO_3^- influences the geometrical structures of NPrC, NC·NC, and NC·AC.

Acknowledgment. I thank Professor Fumio Hirayama for his valuable discussion.

Counterion Surface Diffusion in a Lyotropic Mesophase. A ^{23}Na Two-Dimensional Quadrupolar Echo NMR Relaxation Study

István Furó,[†] Bertil Halle,* Per-Ola Quist, and Tuck C. Wong[‡]

Physical Chemistry 1, University of Lund, Chemical Center, P.O. Box 124, S-22100 Lund, Sweden

(Received: July 12, 1989)

In the first systematic application of the two-dimensional quadrupolar echo (2DQE) method, we study the ^{23}Na NMR relaxation behavior of counterions in the reversed hexagonal mesophase of the AOT/ D_2O /isooctane system, consisting of long cylindrical aggregates with the water and ions on the inside. Using a combination of relaxation experiments, performed on magnetically aligned samples, we determine the three spectral densities at two sample orientations. The orientational dependence of the spectral densities allows us to separate contributions from different types of molecular motion. In particular, we find a dominant contribution from surface diffusion of counterions along the periphery of the cylindrical aqueous regions (diameter ca. 50 Å). From the frequency dependence of this contribution, we determine the diffusion coefficient of sodium ions in the interfacial region, a quantity which is important for a variety of phenomena in colloid and polymer science, electrochemistry, and biophysics. We thus obtain $D(\text{Na}^+) = (2.8 \pm 0.3) \times 10^{-10} \text{ m}^2 \text{ s}^{-1}$, which is a factor of 3.6 lower than in an infinitely dilute aqueous (D_2O) electrolyte solution at the same temperature (20.6 °C). In addition, our analysis of the ^{23}Na relaxation rates and spectral line shapes provides information about the fast local ion and water dynamics in the interfacial region, as well as about the equilibrium structure of the liquid crystalline phase.

Introduction

The technique of nuclear spin relaxation is one of the most versatile and powerful tools available for the study of molecular organization and dynamic processes in complex fluids. Among the variety of useful magnetic isotopes, the quadrupolar nuclei of atomic ions, such as ^{23}Na , have found extensive use, mainly in the polyelectrolyte and surfactant fields¹ and in biophysics.^{2,3} The more recent applications include studies of synthetic polyelectrolytes,⁴⁻⁶ DNA,^{7,8} and polysaccharides^{9,10} as well as more complex biological systems.¹¹⁻¹³

Virtually all previous counterion spin relaxation work has been devoted to isotropic solution systems. In locally heterogeneous isotropic fluids, the fluctuations that drive the relaxation of the spin system are distributed over many, often quite complex, degrees of freedom of the molecular system. While this complexity enhances the information content of the spin relaxation rates, it can also become an obstacle on the, often long and treacherous, path to a unique interpretation.

One strategy for avoiding interpretational ambiguities is to study systems that are simpler in structure, yet exhibit the essential

features of interest, e.g., an electrolyte solution interface. In this work we have adopted this strategy, by choosing to study a lyotropic liquid crystalline mesophase. Being translationally and orientationally ordered over macroscopic dimensions, smectic liquid crystals offer the prospect of a relatively straightforward interpretation of relaxation data, provided that appropriate relaxation experiments can be designed and implemented. This is particularly

(1) Lindman, B. In *NMR of Newly Accessible Nuclei*; Laszlo, P., Ed.; Academic Press: New York, 1983; Vol. 1, p 193.

(2) Gupta, R. K.; Gupta, P.; Moore, R. D. *Annu. Rev. Biophys. Bioeng.* **1984**, *13*, 221.

(3) Springer, C. S. *Annu. Rev. Biophys. Chem.* **1987**, *16*, 375.

(4) Levij, M.; de Bleijser, J.; Leyte, J. C. *Chem. Phys. Lett.* **1981**, *83*, 183; **1982**, *87*, 34.

(5) Halle, B.; Wennerström, H.; Piculell, L. *J. Phys. Chem.* **1984**, *88*, 2482.

(6) Halle, B.; Bratko, D.; Piculell, L. *Ber. Bunsen-Ges. Phys. Chem.* **1985**, *89*, 1254.

(7) Nordenskiöld, L.; Chang, D. K.; Anderson, C. F.; Record, M. T. *Biochemistry* **1984**, *23*, 4309.

(8) van Dijk, L.; Gruwel, M. L. H.; Jesse, W.; de Bleijser, J.; Leyte, J. C. *Biopolymers* **1987**, *26*, 261.

(9) Grasdalen, H.; Kvam, B. J. *Macromolecules* **1986**, *19*, 1913.

(10) Piculell, L.; Nilsson, S. *J. Phys. Chem.* **1989**, *93*, 5602.

(11) Monoi, H. *Biophys. J.* **1985**, *48*, 643.

(12) Pettegrew, J. W.; Glonek, T.; Minshew, N. J.; Woessner, D. E. *J. Magn. Reson.* **1985**, *63*, 439.

(13) Urry, D. W. *Bull. Magn. Reson.* **1987**, *9*, 109.

[†] On leave from the Central Research Institute for Physics, Budapest, Hungary.

[‡] Present address: Department of Chemistry, University of Missouri, Columbia, MO 65211.

true for the many lyotropic mesophases, whose regular arrangement of surfactant aggregates have been accurately characterized by X-ray diffraction.¹⁴

The particular system under study here is the reversed hexagonal (F) phase in the AOT/D₂O/isooctane system (AOT = sodium bis(2-ethylhexyl) sulfosuccinate), consisting of hexagonally arranged cylindrical aggregates, with water and sodium ions on the inside and a continuous hydrocarbon region on the outside.¹⁵ A useful feature of this system is that the radius of the aqueous rods can be varied, without altering the local properties of the interface, simply by changing the relative amounts of water and AOT.

While quadrupolar splittings from counterions in lyotropic mesophases have been studied extensively,^{1,16} we are not aware of any systematic studies of counterion relaxation in such systems. One can discern several reasons for the scarcity of counterion relaxation studies on anisotropic systems. One major reason is related to the fact that, while the structure and molecular dynamics are usually simpler in anisotropic than in isotropic heterogeneous systems, the reverse is true for the spin dynamics, particularly for nuclei with spin $I > 1$ (as for virtually all counterion nuclei). However, as the spin system can be extensively manipulated by coherent radio-frequency (rf) pulses, the complicated spin dynamics need not be a problem. In fact, it can be turned into an advantage.

We have recently embarked on a program for designing multiple-pulse techniques to study quadrupolar relaxation of high-spin nuclei in anisotropic systems.¹⁷⁻²⁰ Of particular relevance for the present study is the two-dimensional quadrupolar echo (2DQE) method,¹⁷ which allows the zero-frequency spectral density (which is sensitive to motions on a time scale of $>10^{-9}$ s) to be determined from the spectral satellites, in spite of static inhomogeneity broadening due to a residual orientational disorder and/or a spatially nonuniform quadrupole coupling constant. In the system studied here, both kinds of sample inhomogeneity are present and contribute substantially to the satellite line width in the ²³Na spectrum. Under such conditions, the 2DQE experiment is an indispensable tool for an accurate determination of the homogeneous line width. (A direct line shape fit to the conventional spectrum²¹ cannot distinguish a symmetric inhomogeneity broadening, as produced by a nonuniform quadrupole coupling, from the homogeneous line width.) Since this study represents the first systematic application of the 2DQE method, we shall devote some attention to methodological aspects.

Another potential problem with relaxation studies on anisotropic systems is the need to induce, e.g., by a strong magnetic field, a (preferably, enduring) macroscopic alignment in the NMR sample. In principle, relaxation data from unaligned (powder) samples contain information about the orientational dependence of the spectral densities. In practice, however, this information is often difficult to extract from the powder spectra (cf. below). Fortunately, the reversed hexagonal phase under study here can be magnetically aligned, so the orientation-dependent spectral densities can be readily determined. In effect, we exploit the tensorial nature of the nuclear quadrupole coupling to selectively monitor different motional degrees of freedom on the basis of their symmetry properties.

The analysis of our ²³Na NMR data is divided into two parts. First we deal with static properties, such as sample morphology, orientational (dis)order, counterion distribution, and residual quadrupole coupling constant. These properties, which also have a bearing on the relaxation data, are deduced from an analysis

TABLE I: Composition, Structure, and Phase Transition Temperature of Investigated F-Phase Samples

	sample			
	I	II	III	IV
wt % isooctane	13.0	13.1	13.0	13.4
x (mol D ₂ O/mol AOT)	18.0	20.9	24.4	27.3
cylinder radius, R/Å	22.6	25.3	28.5	31.2
phase transition ^a temp/°C	28	30	32	33
nonaligned fraction, f	0.21	0.25	0.23	0.21

^a The F and L₂ phases coexist in a 1–2 °C range around the given phase transition temperature.

of spectral line shapes and quadrupolar line splittings. In the second part, we analyze the various relaxation rates. As a first step, we convert the relaxation rates into orientation-dependent spectral densities. These are further decomposed, using a recently developed general theoretical framework²² for spin relaxation by translational diffusion in ordered fluids, into reduced spectral densities, associated with motions of different symmetry and on different time scales. Apart from the ubiquitous fast local motions, there is a dominant contribution from lateral counterion diffusion along the cylindrical interface (around the cylindrical axis). The frequency dependence of this contribution yields directly the associated correlation time. By repeating the whole procedure for samples of different water/surfactant molar ratio, we can accurately determine the translational self-diffusion coefficient for sodium ions in the interfacial region.

For the sake of continuity in presentation, we have relegated most derivations and technical considerations to five appendices.

Materials and Sample Preparation

AOT (sodium bis(2-ethylhexyl) sulfosuccinate) from Sigma and isooctane (2,2,4-trimethylpentane) from Aldrich (99%) were used as supplied. The water was a 4:1 mixture of D₂O (>99.8% ²H) from Norsk Hydro and ¹⁷O-enriched D₂O (22% ¹⁷O, 62% ¹⁸O) from Ventron. (The ¹⁷O enrichment was motivated by a parallel water ¹⁷O relaxation study, to be reported elsewhere, of our F-phase samples. The deviation from the natural oxygen isotope composition has no significant effect on the ²³Na NMR data.)

Samples in the reversed hexagonal (F) phase of the AOT/D₂O/isooctane system were prepared by weighing the components into 10-mm-o.d. Pyrex tubes (cleaned with alkaline ethanol and rinsed with doubly distilled water), which were then flame-sealed. The samples were homogenized by shaking at 40 °C, where they exist in the form of an isotropic microemulsion (L₂) phase (cf. phase transition temperatures in Table I), which has a much lower viscosity than the F phase. The samples were then brought into the F phase by cooling. The resulting liquid crystal powder samples (containing randomly oriented crystalline domains) were identified optically between crossed polarizers and through their characteristic ²H NMR quadrupolar powder spectra.

Macroscopically aligned F-phase samples were prepared by slow cooling in the presence of a magnetic field ($B_0 = 8.5$ T). The F phase has a positive magnetic susceptibility anisotropy and is consequently aligned with the director of the uniaxial phase parallel to the magnetic field. Once induced by the magnetic field, the macroscopic orientation persists (cf. below), thus allowing NMR experiments to be carried out at nonzero angle θ_{LD} between the magnetic field and the phase director. No change in the ²³Na relaxation data could be detected after storing the samples at 5 °C (still in the F phase) for up to 2 months. To prevent the aligned samples from flowing during measurements in the horizontal NMR probe (see below), the tubes were opened and a Teflon plug was tightly fitted at the liquid crystal/air interface. The measurements with this probe were then completed within 24 h. An air-flow temperature controller provided ± 0.3 °C sample temperature stability (measured with a thermocouple) during the measurements.

(22) Halle, B. *Mol. Phys.* **1987**, *60*, 319. There is a misprint in eq 2.34, the last term of which should read $F_{k2}(\theta_{LC})\hat{J}_2^2(\omega)$.

(14) Fontell, K. In *Liquid Crystals and Plastic Crystals*; Gray, G. W., Winsor, P. A., Eds.; Ellis Horwood: Chichester, 1974; Chapter 4.

(15) Ekwall, P.; Mandell, L.; Fontell, K. *J. Colloid Interface Sci.* **1970**, *33*, 215.

(16) Boden, N.; Jones, S. A. In *Nuclear Magnetic Resonance of Liquid Crystals*; Emsley, J. W., Ed.; D. Reidel: Dordrecht, 1985; p 473.

(17) Furó, I.; Halle, B.; Wong, T. C. *J. Chem. Phys.* **1988**, *89*, 5382.

(18) Furó, I.; Halle, B. *J. Chem. Phys.* **1989**, *91*, 42.

(19) Furó, I.; Halle, B.; Einarsson, L. *J. Magn. Reson.*, in press.

(20) Furó, I.; Halle, B. Unpublished results.

(21) Chachaty, C.; Quagebeur, J. P. *Mol. Phys.* **1984**, *52*, 1081.

NMR Methodology

All NMR measurements were performed on a Bruker MSL-100 spectrometer (^{23}Na resonance frequency 26.49 MHz), equipped with a saddle-coil vertical 10-mm probe (for measurements at $\theta_{\text{LD}} = 0^\circ$) and a solenoidal horizontal 10-mm probe (for measurements at $\theta_{\text{LD}} = 90^\circ$). The ^{23}Na 90° pulse length was 6–7 μs , which provided sufficiently uniform excitation in the quadrupole-split spectra. This was confirmed by the finding that the central line and the satellites were fully inverted by rf pulses of virtually the same length (to within 0.3 μs).

Inversion Recovery. The satellite longitudinal relaxation rate, $R_{1s} = 1/T_{1s}$, was determined from a conventional inversion recovery experiment, using 23 delay times in the range $(0.1-10)T_{1s}$. A least-squares fit of the recovery function $h = h_0[1 - a \exp(-R_{1s}\tau)]$ to the satellite peak amplitude h versus delay time τ yielded R_{1s} . Reported R_{1s} values represent averages over the two satellites. Since the central line inversion recovery is biexponential,¹⁸ it is unsuitable for accurate determination of relaxation rates. A further complication in our samples is the contribution to the central line intensity from the nonaligned part of the sample (cf. below). Consequently, we analyze the inversion recovery of the satellites only.

2D Hahn Echo. The homogeneous central line width $\Delta\nu_c^{\text{hom}}$, and the corresponding relaxation rate $R_c^{\text{hom}} = \pi\Delta\nu_c^{\text{hom}}$, was determined from a 2D FT Hahn echo experiment,^{19,23} using the pulse sequence $(\pi/2)_x - \tau - (\pi)_y - \tau - \text{acq}$ with 64 τ values and a narrow (2–3 kHz) filter width. R_c^{hom} was obtained from a Lorentzian fit to the homogeneous central line in the F1 cross-section spectrum resulting from Fourier transformation with respect to τ (with zero filling to 4 K) of the peak amplitude of the inhomogeneous central line in the F2 spectrum. We also determined the inhomogeneous central line width $\Delta\nu_c^{\text{inhom}}$ in the conventional (single $\pi/2$ pulse) 1D spectrum. The difference $\Delta\nu_c^{\text{inhom}} - \Delta\nu_c^{\text{hom}}$, which is due to magnetic field inhomogeneity, was less than 15 and 45 Hz for the vertical and horizontal probes, respectively.

2D Quadrupolar Echo. The homogeneous satellite line width $\Delta\nu_s^{\text{hom}}$, which reports on slow molecular processes via the zero-frequency spectral density, cannot be accurately determined from the conventional 1D spectrum, the satellites of which are severely broadened by sample inhomogeneity (of the local director orientation θ_{LD} and of the motionally averaged quadrupole coupling constant). This problem can be circumvented by using the 2D quadrupolar echo (2DQE) method,¹⁷ wherein the quadrupolar dephasing due to sample inhomogeneity is refocused by the pulse sequence $(\pi/2)_x - \tau - (\pi/2)_y - \tau - \text{acq}$. Fourier transformation with respect to τ of the peak amplitudes of the inhomogeneous lines in the F2 spectrum yields F1 cross-section spectra, the central line width of which directly provides the homogeneous (unaffected by sample inhomogeneity) width of the corresponding F2 lines. We denote by R_c^{QE} and R_s^{QE} the relaxation rates obtained by the 2DQE method using the central line or the satellite line, respectively, in the F2 spectrum.

Since this is the first systematic application of the 2DQE method, it is appropriate to give an account of some of the technicalities involved in this experiment. In the first step, we generate a 1D QE (or F2) spectrum (1–2 K) by Fourier transforming the free induction decay, starting at the echo a time τ after the second QE pulse. As in the spin $I = 1$ case,²⁴ the effect of the finite length of the rf pulses on the echo position has to be corrected for. This was done empirically by shifting the starting point for the acquisition period by about the pulse length. For the special choice of delay time $\tau = 1/\nu_Q$, where ν_Q is the quadrupolar splitting, the F2 spectrum is identical with the conventional (single $\pi/2$ pulse) 3:4:3 pure absorption-mode spectrum, as shown in Figure 1a. F2 spectra, with τ -dependent phase and amplitude, were recorded for 256 or 512 different τ values. Since we only need the central line in the F1 spectra to determine R_c^{QE} and R_s^{QE} , and since the quadrupolar splitting is halved in the F1 dimension (cf. Figure 1), a relatively small spectral width, and corre-

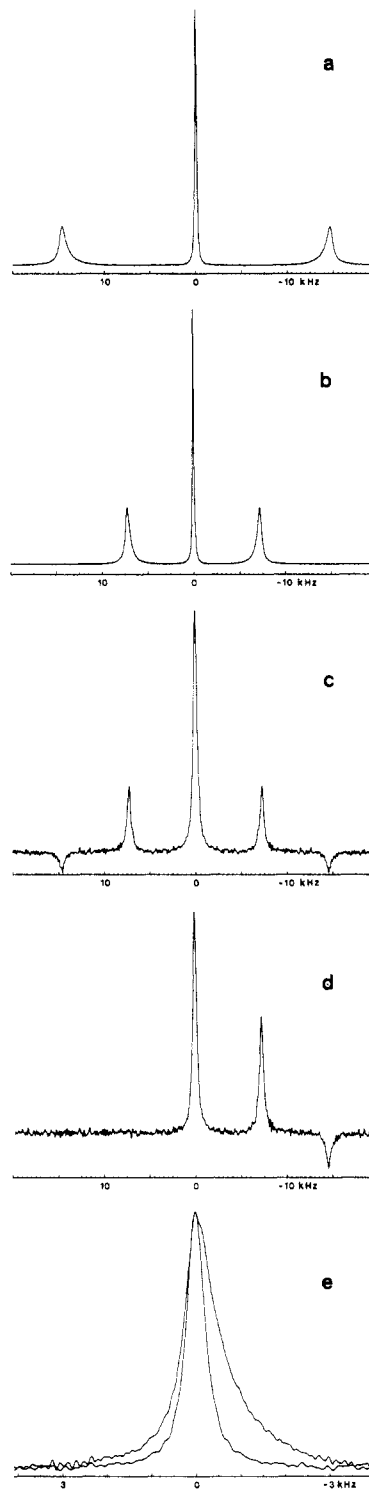


Figure 1. ^{23}Na 2DQE spectra from sample IV ($T = 20.6^\circ\text{C}$) oriented at $\theta_{\text{LD}} = 90^\circ$. (a) Conventional (F2) spectrum produced with the QE sequence for $\tau = 1/\nu_Q$, where $\nu_Q = 14.45\text{ kHz}$ is the quadrupolar splitting. The relative line intensities are 3:4:3. The full widths at half-amplitude are 201 and 950 Hz for the central line and the satellites, respectively. (b) F1 cross-section spectrum $L(\omega_1, 0)$, obtained by Fourier transformation with respect to τ of the amplitude at the position of the central line in (a). The relative line intensities are 3:2:3. The splitting is reduced to half of that in (a), and the central line width is 168 Hz. (c) F1 cross-section spectrum $L(\omega_1, \omega_Q)$, obtained by Fourier transformation of the amplitude at the position of a satellite in (a). The relative line intensities are -1:2:6:2:-1. The splitting is reduced to half of that in (a), and the central line width is 489 Hz. (d) Asymmetric $L(\omega_1, \omega_Q)$ spectrum, obtained after two complex Fourier transforms (see text). The relative line intensities are 3:2:-1, and the line widths are the same as in (c). (e) The central line in (c) superimposed on a satellite in (a). The homogeneous line width is the same in both cases, but due to sample inhomogeneity, the F2 satellite is nearly twice as broad as the F1 central line.

(23) Hahn, E. L. *Phys. Rev.* **1950**, *80*, 580.

(24) Bloom, M.; Davis, J. H.; Valic, M. I. *Can. J. Phys.* **1980**, *58*, 1510.

spondingly large τ increment, could be used. To avoid receiver dead time distortion, the smallest τ value was $1/\nu_Q$. The phases have to be set accurately and must be stable (to within 2–3°) for the duration of the experiment (typically 10–15 h). Further, a large filter width should be used, to avoid distortion of the satellite decay.

Fourier transformation with respect to τ of the amplitude at $\omega_2 = 0$ yields, after zero filling to 8 K and phase correction, the 3:2:3 F1 cross-section spectrum $L(\omega_1, 0)$, shown in Figure 1b. From the width of the central line in this spectrum, we obtain the relaxation rate R_c^{QE} . Similarly, Fourier transformation of the amplitude at $\omega_2 = \omega_Q$ (defined by the satellite position in the $\tau = 1/\nu_Q$ F2 spectrum) yields the -1:2:6:2:-1 F1 cross-section spectrum $L(\omega_1, \omega_Q)$, shown in Figure 1c. From the central line width, we obtain R_s^{QE} .

In practice, the $L(\omega_1, \omega_Q)$ spectrum was obtained as follows. The phase of the second QE pulse was alternated between $+y$ and $-y$. With proper phase setting, and with the central line exactly on resonance, the out-of-phase spectrometer channel then contains only noise,^{17,20} which can be zeroed to improve the signal-to-noise ratio. After two complex Fourier transforms, the absorption channel of the quadrature detector contains the asymmetric F1 spectrum shown in Figure 1d. The F1 line at $\omega_1 \approx 0$ is, in fact, slightly shifted from $\omega_1 = 0$, due to a second-order dynamic shift and/or to an asymmetric distribution of magnetic field or residual quadrupole coupling constant.²⁰ Consequently, the spectrum was first shifted to $\omega_1 = 0$ and then symmetrized by adding a frequency-reversed spectrum, resulting in the $L(\omega_1, \omega_Q)$ spectrum in Figure 1c. This procedure yields a higher signal-to-noise ratio than the single-channel Fourier transforms used to illustrate the 2DQE method in ref 17.

The usefulness of the 2DQE method is evident from Figure 1e, showing the central line in the $L(\omega_1, \omega_Q)$ spectrum superimposed on one of the satellites in the F2 spectrum of Figure 1a. The large broadening and asymmetry of the latter, essentially due to sample inhomogeneity (see below), clearly prevent a determination of the homogeneous satellite line width. The central F1 line, however, directly yields the homogeneous satellite line width, except for a (relatively small) symmetric broadening due to magnetic field inhomogeneity. In principle, this residual broadening could be eliminated by using the modified QE sequence¹⁷ $(\pi/2)_x - \tau/2 - (\pi)_y - \tau/2 - (\pi/2)_y - \tau/2 - (\pi)_y - \tau/2 - \text{acq.}$ Since the introduction of two 180° pulses, which, on account of the large splitting, are not perfectly nonselective, produced some spectral distortion, we refrained from using this sequence. However, as we will need only the difference $R_s^{QE} - R_c^{QE}$ (see below), the field inhomogeneity broadening is essentially canceled out. This is true as long as the magnetic field inhomogeneity broadening is small compared to the homogeneous line width.¹⁷

Relaxation in Powder Samples. The relaxation experiments described above were performed on macroscopically aligned samples as well as on powder samples. Since the relaxation rates are orientation dependent, the two kinds of sample, in principle, furnish complementary information. For the large quadrupolar splittings in our samples, however, the broad spectral distribution of the satellite line intensity limits the accuracy with which the true powder relaxation rates can be determined. This is particularly true for the rates derived from the satellites, since the signal-to-noise ratio at the satellite peak position is much lower in the powder samples than in the aligned samples. The inversion recovery of the central line, even in the case of a magic-angle detection pulse,¹⁸ is complicated to analyze since it is rendered nonexponential by the orientational dependence of the nonsecular spectral densities. The zero-frequency spectral density is even more difficult to determine for powder samples. Thus, the R_s^{QE} experiment is not only plagued by a low signal-to-noise ratio but is further complicated by interference from the overlapping companion satellite, which mixes in a relaxation contribution corresponding to $\theta_{LD} = 35.26^\circ$. For these reasons, we shall restrict the analysis to relaxation data obtained from macroscopically aligned samples. We note, however, that, within the experimental uncertainty, the powder relaxation data are consistent with the

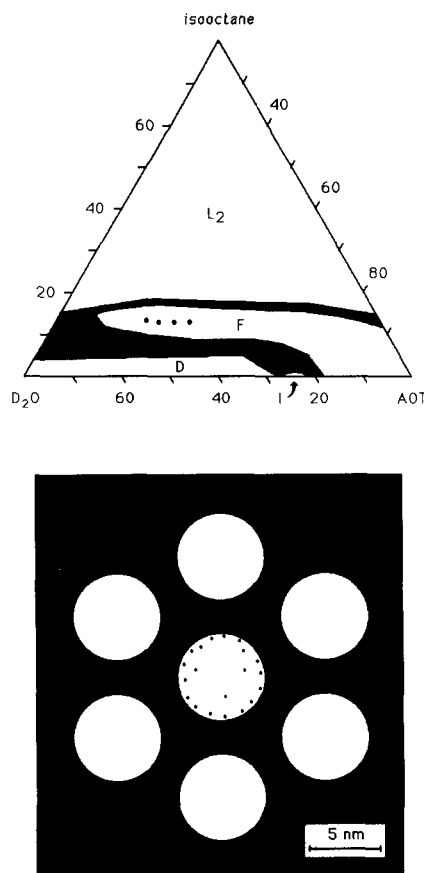


Figure 2. Partial phase diagram (top) of the system AOT/D₂O/isooctane at 20 °C, roughly showing the one-phase regions of the isotropic microemulsion (L₂) phase and the lamellar (D), cubic (I), and reversed hexagonal (F) liquid crystalline phases. (Note that the diagram does not cover the entire composition space.) The dots correspond to the composition (weight percent) of the four investigated samples. The lower part of the figure is a cross-sectional view, drawn to scale, of the hexagonally arranged aqueous cylinders in sample IV. The shaded region contains AOT hydrocarbon chains and isooctane, while the water, sodium counterions, and sulfonate headgroups reside inside the cylinders. The counterion distribution is qualitatively as shown in the central cylinder, with about 85% of the ions within 5 Å of the interface.

orientation dependence of the relaxation rates measured on aligned samples.

Static Properties

Before analyzing the ²³Na relaxation rates, it is necessary to examine certain static properties of our F-phase samples, such as the phase structure and the extent of magnetic-field-induced alignment. This static information can be obtained from an analysis of quadrupolar splittings and line shapes. The residual quadrupole coupling constant, deduced from the splitting, will also be of relevance for the interpretation of the relaxation data.

F-Phase Structure. In its pure state, the anionic surfactant AOT forms a mesophase with a unit cell consisting of hexagonally arranged, long parallel rodlike aggregates with the sulfonate headgroups and sodium counterions confined to the central core of the rod.¹⁵ The core can incorporate water up to $x = 5$ –6. (Throughout this paper, we use x to denote moles of water per mole of AOT.) If a third nonpolar component is added, it forms, together with the AOT hydrocarbon chains, a continuous oil region, thus increasing the rod separation while maintaining the hexagonal symmetry. This reversed hexagonal liquid crystalline mesophase (denoted F) can incorporate more water, forming aqueous rods with the AOT headgroups at the cylindrical (or nearly so) oil/water interface.

The ternary-phase diagrams of several AOT/water/oil systems have been partially determined.^{15,25–27} The approximate

TABLE II: ^{23}Na Quadrupolar Splittings from F-Phase Samples at 20.6 °C

	sample			
	I	II	III	IV
$\nu_Q(\theta_{\text{LD}}=0^\circ)^a/\text{kHz}$	33.05	31.52	30.08	28.93
$\nu_Q(\theta_{\text{LD}}=90^\circ)^a/\text{kHz}$	16.52	15.78	15.06	14.45
$\nu_Q(\theta_{\text{LD}}=0^\circ)/\nu_Q(\theta_{\text{LD}}=90^\circ)$	2.000	1.997	1.997	2.002
$\nu_Q(\text{powder})^a/\text{kHz}$	16.48	15.68	14.99	14.54

^a Estimated uncertainty ± 50 Hz.

extensions of the F phase, and of the adjacent lamellar (D) and microemulsion (L_2) phases, are indicated in Figure 2 for the investigated AOT/ D_2O /isooctane system at 20 °C. NMR studies were performed on four F-phase samples (labeled I–IV), the compositions of which are given in Table I and shown in Figure 2. With increasing temperature, the lower boundary of the isotropic L_2 phase is displaced toward lower isooctane fractions, so that, above about 30 °C (cf. Table I), our samples are isotropic.

The radius R of the aqueous rods is determined essentially by the water/AOT molar ratio x . If we assume that all AOT molecules reside at the cylindrical water/hydrocarbon interface of very long (end effects neglected) aqueous rods, then the geometry dictates that

$$R = (2v_w/a_s)x + R_s \quad (1a)$$

where v_w is the volume per water molecule and a_s is the interfacial area per AOT molecule. R_s is related to the volume of the surfactant headgroup (including the counterion), but its precise value depends on where one chooses to locate the interface between the polar and nonpolar regions. The three quantities v_w , a_s , and R_s are expected to vary with x at low water content and to attain constant values only above a certain level of hydration, $x > x_0$. From X-ray diffraction studies¹⁵ of the F phase in the system AOT/ H_2O / p -xylene at 20 °C, we know that $a_s^0 = 65 \text{ \AA}^2$ for $x > 10$. (The superscript zero signifies the x -independent limit.) Further, the water added to the central part of the aqueous core should behave essentially as bulk water for $x > 15$, as recently demonstrated²⁸ for water droplets in the L_2 phase. Hence, $v_w^0 = 30 \text{ \AA}^3$ at 20 °C. For $x > x_0 \approx 15$, eq 1a may thus be expressed as

$$R = (2v_w^0/a_s^0)x + R'_s \quad (1b)$$

where R'_s now accounts also for any deviations at $x < x_0$ of v_w and a_s from their limiting values. As shown below, our molecular interpretation of the ^{23}Na relaxation data does not require the value of R'_s to be specified. However, in order to estimate the radial distribution of the counterions within the aqueous region, we need to know roughly what the cylinder radius is. For this purpose only, we shall use the value $R'_s = 6 \text{ \AA}$, which is reasonable but subject to some uncertainty. The radii obtained in this way for our four samples are given in Table I. Figure 2 also shows a cross-sectional scale drawing of sample IV, with the rod spacing given by the composition and bulk densities.

Orientalional Order. For each of the four F-phase samples, three series of NMR measurements were carried out, viz., on powder samples (with the crystalline domains randomly oriented with respect to the static magnetic field, B_0) and on magnetically aligned samples in two probe configurations corresponding to $\theta_{\text{LD}} = 0^\circ$ and $\theta_{\text{LD}} = 90^\circ$, where θ_{LD} is the angle between the lab-fixed B_0 field and the phase director. The orientational dependence of the ^{23}Na quadrupolar splitting ν_Q is governed by the second-rank Legendre polynomial,²⁹ i.e.

$$\nu_Q \propto |3 \cos^2 \theta_{\text{LD}} - 1| \quad (2)$$

Hence, we expect that the splitting in the $\theta_{\text{LD}} = 0^\circ$ configuration should be twice as large as that obtained for $\theta_{\text{LD}} = 90^\circ$. As seen

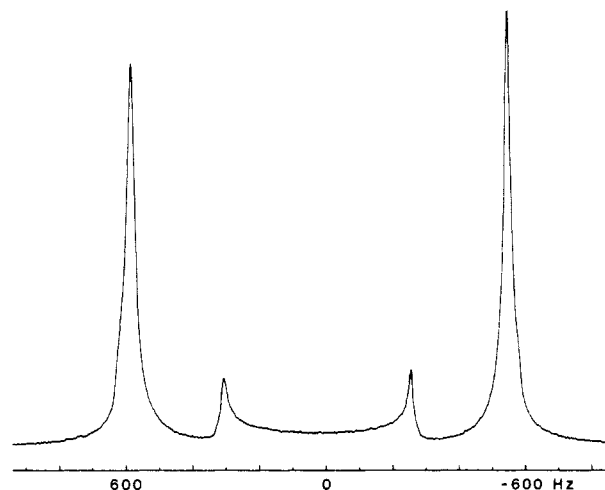


Figure 3. Water ^2H spectrum of sample I oriented at $\theta_{\text{LD}} = 0^\circ$, showing superposition of spectra from magnetically aligned and nonaligned parts of the sample.

from Table II, the data conform closely to eq 2. In powder samples the most probable polar angle is $\theta_{\text{LD}} = 90^\circ$. Provided that the powder splitting is much larger than the line width, it should thus coincide with the splitting from the aligned sample with $\theta_{\text{LD}} = 90^\circ$. According to Table II, this is indeed the case.

Although the samples were readily and reproducibly aligned on cooling from the L_2 phase in a magnetic field of 8.5 T, it was always found that 20–25% of the sample did not respond to the field. This is most clearly seen in the water ^2H spectrum recorded in the $\theta_{\text{LD}} = 0^\circ$ configuration (Figure 3). In addition to the dominating doublet, corresponding to the aligned part of the sample, there is a smaller powderlike contribution with half of the $\theta_{\text{LD}} = 0^\circ$ splitting. The integrated intensity of the latter contribution corresponds to a nonaligned fraction of 0.21. Similar results were obtained with the other three samples (Table I). Two minor features of the main doublet in Figure 3 may be noted: (i) the slight difference in peak intensities and (ii) the shoulders on the outer flanks. Without having made a systematic study of these features, we tentatively ascribe them to magnetic field and sample inhomogeneity, respectively. The shoulders in the ^2H spectrum disappear with time (cf. below) and, moreover, are not seen in the ^{23}Na spectra.

From the splitting ratio (2.02), we conclude that the nonaligned fraction consists either of randomly oriented crystalline domains or of domains preferentially oriented perpendicularly to the axis of the sample tube (and the magnetic field), but with some spread around the preferred orientation to account for the line shape asymmetry. (In the latter event, also the powder samples should be orientationally inhomogeneous.) These two cases could be distinguished by a detailed line shape analysis (requiring knowledge of the homogeneous ^2H line width) or by establishing the presence of the outer satellites of the characteristic 2D powder line shape³⁰ in the $\theta_{\text{LD}} = 90^\circ$ configuration. As this distinction is unimportant for the analysis of the ^{23}Na relaxation data (see below), the matter will not be pursued further here. It is worth noting, however, that we obtained a larger nonaligned fraction in sample containers with a larger surface-to-volume ratio, indicating that the nonaligned domains are located at the glass wall of the sample tube. For an inner tube diameter of 7 mm and a nonaligned fraction of 0.25, the range of the wall effect must then be about 0.5 mm. It should also be noted that the nonaligned fraction decreases with time. The spectrum shown in Figure 3 was recorded about 1 h after the alignment was induced. Another ^2H spectrum, taken after the sample had been stored for about 2 months at 5 °C, yielded a nonaligned fraction of only 0.03 (and the shoulders in the spectrum had disappeared.) Hence, after the initial alignment of 75% of the sample as the two-phase region is traversed, there is apparently a slow process whereby small peripheral domains

(26) Tamamushi, B.; Watanabe, N. *Colloid Polym. Sci.* **1980**, *258*, 174.

(27) Stilbs, P.; Lindman, B. *J. Colloid Interface Sci.* **1984**, *99*, 290.

(28) Carlström, G.; Halle, B. *Langmuir* **1988**, *4*, 1346.

(29) Abragam, A. *The Principles of Nuclear Magnetism*; Clarendon Press: Oxford, U.K., 1961.

(30) Forrest, B. J.; Reeves, L. W. *Chem. Rev.* **1981**, *81*, 1.

TABLE III: Sample Inhomogeneity As Deduced from Satellite Line Shapes

	sample			
	I	II	III	IV
rel qcc spread, 100 ϵ	0.5	0.4	0.5	0.6
rel x spread, 100 $\Delta x/x$	1.4	1.4	1.4	1.6
θ_{LD} spread, σ /deg	5	5	7.5	7
rel line shift, 100 $\Delta\nu_Q/\bar{\nu}_Q$	-0.2	-0.3	-0.3	-0.4

are aligned with, and incorporated into, the central aligned domain.

Even in the macroscopically aligned part of the sample, there is a certain orientational disorder. It is this fact, clearly revealed by the broadening and asymmetry of the inhomogeneous satellite in Figure 1e, which prompted us to measure transverse relaxation by the 2DQE method. Since the relaxation rates are orientation dependent (see below), it is important to quantify this orientational disorder.

Sample inhomogeneity is manifested in the NMR spectrum in fundamentally different ways depending on the time scale τ_Q on which the quadrupolar frequency $\omega_Q (=2\pi\nu_Q)$ is averaged by molecular motions. If $\tau_Q \ll (\Delta\omega_Q)^{-1}$, where $\Delta\omega_Q$ is the spread in ω_Q associated with the sample inhomogeneity, then the satellite line is simply a Lorentzian with the homogeneous line width, but the splitting is reduced by the additional motional averaging. If, on the other hand, $\tau_Q \gg (\Delta\omega_Q)^{-1}$, then the inhomogeneity gives rise to a superposition of spectra, each corresponding to a different value of ω_Q . The existence of a macroscopic nonaligned region in the sample (cf. above) is an extreme example of such a static inhomogeneity effect. In our F-phase samples, there is an additional static inhomogeneity effect arising from a continuous distribution of local director orientations θ_{LD} around the mean director orientation $\bar{\theta}_{LD}$ in the aligned region. Such a nonaveraged distribution produces broadening and distortion of the line shape, effects that can be eliminated by using the 2DQE method.^{17,20}

The extent of static θ_{LD} inhomogeneity in our F-phase samples was determined by a numerical line shape fit to the inhomogeneous satellites in the $\bar{\theta}_{LD} = 0^\circ$ spectra (to avoid interference from the nonaligned fraction), using the homogeneous line width determined from the 2DQE experiments. As described in more detail in Appendix A, we assumed a Gaussian θ_{LD} distribution with an orientational spread $\sigma = (\theta_{LD}^2)^{1/2}$. It was found, however, that with a σ value that reproduced the inhomogeneous half-width, the line asymmetry was much larger than observed experimentally. (This was also found for a rectangular θ_{LD} distribution. The outer half of the satellite line shape is, in fact, quite insensitive to the functional form of a narrow θ_{LD} distribution.) We thus concluded that, in addition to the θ_{LD} spread, there is a distribution of motionally averaged quadrupole coupling constants within the sample. When this was allowed for, excellent agreement with the observed line shape was obtained, as illustrated in Figure 4. The orientational spread σ for the four samples was found to be 5–7° (Table III), which evidently is sufficient to render the conventional satellite line shape useless for relaxation measurements. As seen from Table III, the resulting shift of the satellite peaks is very small, which is consistent with the precisely 2-fold reduction of the splitting in going from the $\bar{\theta}_{LD} = 0^\circ$ to the $\bar{\theta}_{LD} = 90^\circ$ configuration.

The relative spread in the quadrupole coupling constant was found to be about 0.5%. (This gave rise to a symmetric line broadening, which was more than an order of magnitude larger than the experimental uncertainty in the homogeneous satellite line width.) We ascribe this spread to a distribution of aqueous cylinder radii within the sample. Using the observed x dependence of the splitting (Table II), we then obtain a relative spread in x of about 1.4%, corresponding to a 0.3–0.5-Å spread in the core radius. Such a small polydispersity would not have been detected in the powder X-ray data.¹⁵ While we can only speculate about the origin of this polydispersity, the observation of a static broadening from this source of about 100 Hz implies that any motional averaging of this inhomogeneity must take place on a time scale longer than 10^{-3} s. If the radius varies along a given aqueous cylinder, then the value of the lateral counterion diffusion

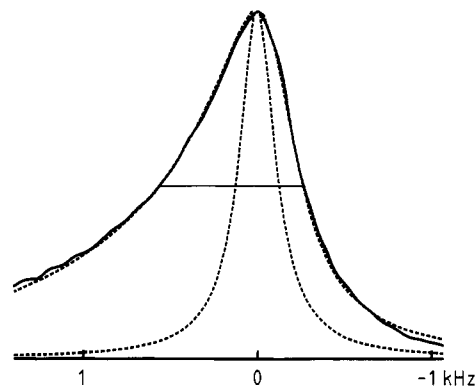


Figure 4. Inhomogeneous satellite line shape (solid curve) from sample IV oriented at $\theta_{LD} = 0^\circ$. The nearly coincident dashed curve was obtained as described in Appendix A, with $\epsilon = 0.006$ and $\sigma = 7^\circ$. The narrow dashed curve is the homogeneous line shape: a Lorentzian with a width of 250 Hz (determined by a 2DQE experiment).

coefficient (determined in the following) implies that the radius fluctuations persist over a length scale of at least 10^{-6} m, which seems improbable. Since the residence time of a counterion within a cylinder is likely³¹ to exceed 10^{-3} s, it is more plausible that the static broadening is due to a slight variation of the water/AOT ratio within the sample.

Residual Quadrupole Coupling. The ^{23}Na quadrupolar splitting ν_Q is a consequence of the interaction of the nuclear quadrupole moment with the electric field gradient generated by the surrounding charge distribution. Since a counterion in the F phase is in an anisotropic environment, molecular motions cannot average out the quadrupole coupling completely, as in an isotropic solution. The resulting ^{23}Na quadrupolar splitting is given by

$$\nu_Q = (1/4)(3 \cos^2 \theta_{LD} - 1)\langle \chi \rangle_D \quad (3)$$

where $\langle \chi \rangle_D$ is the quadrupole coupling constant (qcc), expressed in the local director frame (D) and averaged by all molecular motions (cf. below) taking place on a time scale shorter than the inverse of the splitting difference which they average. (Since the sign of ν_Q cannot be determined experimentally, we define ν_Q as a positive quantity.)

It is convenient to explicitly perform the spatial averaging brought about by counterion diffusion within the cylindrical region of radius R . Hence

$$\langle \chi \rangle_D = (1/2) \int_0^R dr 2\pi r n(r) \bar{\chi}(r) / \int_0^R dr 2\pi r n(r) \quad (4)$$

where $n(r)$ is the local counterion density and $\bar{\chi}(r)$ is the "local" qcc, averaged over all degrees of freedom except for radial diffusion. The factor 1/2 in eq 4 results from averaging by lateral counterion diffusion (cf. below). Since the residual electric field gradient is a short-ranged property,³² being determined essentially by the surface-induced asymmetry in the primary hydration shell and by (anisotropically distributed) ionic species in the immediate vicinity of the reference ion, the local qcc $\bar{\chi}(r)$ should be essentially zero outside an interfacial layer region of thickness $\delta \ll R$. Hence, we express eq 4 as

$$\langle \chi \rangle_D = \frac{1}{2} P \bar{\chi} \quad (5)$$

where P is the fraction of counterions in the interfacial region $R - \delta < r < R$ and $\bar{\chi}$ (≥ 0 , by definition) is the average of $\bar{\chi}(r)$ in that region. The rationale behind the decomposition of $\langle \chi \rangle_D$ in eq 5 is that $\bar{\chi}$ should be more nearly invariant than $\langle \chi \rangle_D$ with respect to changes in the radial counterion distribution.

If the water/hydrocarbon interface is modeled as a uniformly charged cylindrical surface and the counterions as point charges embedded in a dielectric continuum, then the mean-field coun-

(31) Luisi, P. L.; Giomini, M.; Pileni, M. P.; Robinson, B. H. *Biochim. Biophys. Acta* **1988**, *947*, 209.

(32) Linse, P.; Halle, B. *Mol. Phys.* **1989**, *67*, 537.

TABLE IV: Residual Quadrupole Coupling Constant for Interfacial Sodium Ions

	sample			
	I	II	III	IV
$R/\text{\AA}$	22.6	25.3	28.5	31.2
P^a	0.851	0.843	0.836	0.831
$\bar{\chi}^b/\text{kHz}$	155	150	144	139

^a Fraction counterions within 5 Å of the cylindrical interface, calculated from eq B7 with $a_c(\text{AOT}) = 65 \text{ \AA}^2$, $T = 293 \text{ K}$, and $\epsilon_r(\text{D}_2\text{O}) = 80.1$. ^b Calculated from the quadrupolar splitting ν_Q , using eqs 3 and 5.

terion distribution can be calculated analytically as described in Appendix B. As seen from Table IV, the counterion distribution is highly nonuniform, with about 85% of the ions residing within 5 Å of the charged interface (as compared to 30–40% for a uniform distribution). Since the functions $n(r)$ and $\bar{\chi}(r)$ both increase sharply near the interface, the choice of δ value is not critical. We shall take $\delta = 5 \text{ \AA}$, corresponding roughly to the radius of a hydrated sodium ion. Using the quadrupolar splittings in Table II, we can then calculate the residual qcc $\bar{\chi}$ (motionally averaged within a region extending 5 Å from the interface) from eqs 3 and 5. The result is shown in Table IV. The slight variation of $\bar{\chi}$ with cylinder radius may be an artifact of the approximations used in calculating the fraction P . (A 10% inaccuracy in the primitive-model estimate of P would not be unexpected at $x = 18$, where most water molecules are in contact with AOT head-groups and/or counterions.) Alternatively, the $\bar{\chi}$ variation may be due to slight changes in the counterion distribution within the interfacial region and, hence, to a different sampling of the strongly inhomogeneous function $\bar{\chi}(r)$. Nevertheless, the $\bar{\chi}$ values obtained are in the expected range and are, in fact, quite close to the value 135 kHz deduced⁵ in the same way from ²³Na splittings in the lamellar phase of the binary system AOT/H₂O. As regards the ²³Na splitting, the reversed hexagonal phase differs from the lamellar phase mainly in possessing an additional degree of freedom, namely, counterion diffusion around the rod axis, which reduces the splitting by a factor of 2 (explicitly accounted for in eqs 4 and 5). The close agreement between the $\bar{\chi}$ values thus confirms that our samples are, indeed, in the F phase. We shall return to these qcc results in connection with the analysis of the relaxation data.

Dynamic Properties

We are now ready to address the central issue of this study, namely, the quantitative analysis of the ²³Na relaxation data in terms of molecular motions. For reasons given in the NMR Methodology section, we restrict the analysis to data from macroscopically aligned samples. In the first stage of this analysis, we relate the measured relaxation rates to spectral density functions, which are Fourier transforms of certain time correlation functions of the fluctuating electric field gradient tensor at the counterion nucleus. Making use of known structural properties of the F phase and invoking general symmetry and time scale arguments, we then interpret the spectral densities in terms of the molecular motions taking place within the cylindrical aqueous regions in the F phase. In particular, we are able to accurately determine the lateral self-diffusion coefficient of sodium ions in the interfacial region.

Determination of Spectral Densities. Several types of relaxation experiments, as described in the Methodology section, were performed on macroscopically aligned samples in the $\theta_{\text{LD}} = 0^\circ$ and $\theta_{\text{LD}} = 90^\circ$ configurations. From the relaxation data, collected in Table V, it is immediately apparent that the relaxation is dominated by effects due to the heterogeneous nature of the system. For comparison, the ²³Na relaxation rate in bulk aqueous solutions of simple sodium salts³³ in the concentration range 2–3 mol dm⁻³, corresponding to the mean counterion concentration in the aqueous pseudophase of the F-phase samples, is merely

TABLE V: ²³Na Relaxation Rates^a from Aligned F-Phase Samples at 20.6 °C

	sample			
	I	II	III	IV
$R_{1s}(0^\circ)$	735	660	619	575
$R_{1s}(90^\circ)$	446	408	380	358
$R_c^{\text{hom}}(0^\circ)$	606	566	518	478
$R_c^{\text{hom}}(90^\circ)$	610	559	522	493
$R_c^{\text{QE}}(0^\circ)$	619	566	528	493
$R_c^{\text{QE}}(90^\circ)$	635	597	553	528
$R_s^{\text{QE}}(0^\circ)$	902	854	823	785
$R_s^{\text{QE}}(90^\circ)$	1326	1301	1382	1536

^a All rates in units of s⁻¹. Estimated uncertainties: ± 20 , ± 10 , ± 10 , and $\pm 30 \text{ s}^{-1}$ for R_{1s} , R_c^{hom} , R_c^{QE} , and R_s^{QE} , respectively.

TABLE VI: Orientation-Dependent Spectral Densities^a

	sample			
	I	II	III	IV
$j_0(0^\circ)$	283	288	295	292
$j_0(90^\circ)$	691	704	829	1008
$j_1(0^\circ)$	238	236	208	190
$j_1(90^\circ)$	387	355	332	314
$j_2(0^\circ)$	368	330	310	288
$j_2(90^\circ)$	223	204	190	179

^a All spectral densities in units of s⁻¹. Estimated uncertainties: ± 30 , ± 15 , and $\pm 10 \text{ s}^{-1}$ for j_0 , j_1 , and j_2 , respectively.

20–50 s⁻¹. Further, it is seen that R_{1s} and R_s^{QE} are orientation dependent.

²³Na is a spin $I = 3/2$ nucleus with a large quadrupole moment and is, in the present system, relaxed entirely by the quadrupolar mechanism. The various spin relaxation rates are thus linear combinations of the orientation-dependent spectral densities¹⁷

$$j_k \equiv j_k(k\omega_0; \theta_{\text{LD}}) \\ = \frac{2\pi^2}{3} \left(\frac{eQ}{h} \right)^2 \int_0^\infty dt \cos(k\omega_0 t) G_k(t; \theta_{\text{LD}}), \quad (k = 0, 1, 2) \quad (6)$$

where eQ is the nuclear quadrupole moment, ω_0 is the Larmor frequency, and $G_k(t; \theta_{\text{LD}})$ is the electric field gradient (efg) time correlation function

$$G_k(t; \theta_{\text{LD}}) = \langle [V_k^L(0) - \langle V_k^L \rangle] * [V_k^L(t) - \langle V_k^L \rangle] \rangle \quad (7)$$

where the V_k^L are spherical components in the lab-fixed frame of the second-rank irreducible efg tensor, defined as in ref 34.

In terms of the spectral densities j_k , the satellite longitudinal relaxation rate is given by¹⁸

$$R_{1s} = 2j_2 \quad (8)$$

while the rates obtained from the 2D Hahn echo and 2DQE experiments are^{17,19}

$$R_c^{\text{hom}} = j_1 + j_2 \quad (9)$$

$$R_c^{\text{QE}} = j_1 + j_2 + b \quad (10)$$

$$R_s^{\text{QE}} = j_0 + j_1 + j_2 + b \quad (11)$$

In eqs 10 and 11, b represents the contribution from magnetic field inhomogeneity, which has the same effect on R_c^{QE} and R_s^{QE} if b is small compared to the homogeneous rates,¹⁷ which is the case here.

By substituting the relaxation rates from Table V into eqs 8–11, we can now calculate the spectral densities j_0 , j_1 , and j_2 for the two orientations. From the results in Table VI, it is evident that all three spectral densities are strongly orientation dependent. By coincidence, the sum $j_1 + j_2$ is nearly the same for both orientations, which accounts for the apparent lack of orientation dependence in R_c^{hom} and R_c^{QE} (Table V). In a rotationally invariant (isotropic) system, the spectral density function decreases monotonically with frequency, i.e., $j_0 \geq j_1 \geq j_2$. In an anisotropic

(33) Hertz, H. G.; Holz, M.; Keller, G.; Versmold, H.; Yoon, C. *Ber. Bunsen-Ges. Phys. Chem.* **1974**, *78*, 493.

(34) Halle, B.; Wennerström, H. *J. Chem. Phys.* **1981**, *75*, 1928.

system, however, these inequalities are not necessarily satisfied since the three spectral densities are different functions of orientation and frequency. Thus, for example, we find $j_2 > j_1$ for $\theta_{LD} = 0^\circ$.

As demonstrated above, the NMR line shapes reveal three kinds of sample inhomogeneity: (i) a nonaligned region at the sample boundary, (ii) a distribution of local director orientations θ_{LD} around a mean value $\bar{\theta}_{LD}$, and (iii) a narrow polydispersity in the aqueous cylinder radius. While the radius polydispersity is too small to have a significant effect on the relaxation, the two kinds of orientational disorder may influence the (orientation-dependent) relaxation rates and spectral densities, a complication that was disregarded in the preceding analysis. As in the case of the orientation-dependent quadrupolar frequency $\omega_Q(\theta_{LD})$, the orientation-dependent relaxation rates $R(\theta_{LD})$ are affected in different ways depending on the time scale τ_R on which $R(\theta_{LD})$ is averaged by molecular motions. If $\tau_R \ll (\Delta R)^{-1}$, where ΔR is the spread in $R(\theta_{LD})$ associated with the orientational spread, then the measurements simply yield a motionally averaged relaxation rate $\langle R(\theta_{LD}) \rangle$. If, furthermore, $\tau_R \ll (\Delta \omega_Q)^{-1}$, then there may be an additional contribution to the relaxation rate. Since these motional averaging effects merely alter the interpretation of the spectral densities without affecting their relation to the relaxation rates (i.e., eqs 8–11 remain valid), they will be considered further on in the analysis. At this stage, we need only consider the static effects, for $\tau_R \gg (\Delta R)^{-1}$, of orientational disorder on the measured relaxation rates. As this requires rather lengthy arguments, we refer to Appendix C, where we show that, partly due to fortunate circumstances, the static effects may actually be neglected in the present study.

Interpretation of Spectral Densities. In order to extract useful information from the spectral densities j_k in Table VI, we must identify the molecular degrees of freedom that are responsible for the counterion efg fluctuations and, hence, for the decay of the time correlation function in eq 7. In general, this is a complicated task, which, however, in the present case, can be considerably simplified by invoking known facts about motional time scales (order of magnitude) and about the structure of the F phase. These facts, together with the observed strong orientation dependence, provide the key to a reliable molecular interpretation of the spectral densities.

The molecular motions that are expected to contribute significantly to the counterion efg fluctuation may be divided into two groups on the basis of their time scales. First there are the fast motions, which include small-amplitude dynamics (librations and intermolecular vibrations) within the primary hydration shell of the counterion (on a time scale of 10^{-13} s), as well as collective hydration dynamics and local counterion and AOT headgroup motions (10^{-12} – 10^{-11} s).^{32,35,36} In the group of slow motions, we find radial and lateral (along the cylindrical interface) translational diffusion of the counterion within the cylindrical aqueous region (10^{-10} – 10^{-8} s) and counterion migration among cylinder segments with different orientation with respect to the director (probably, $>10^{-6}$ s). Since these two classes of motions occur on disjoint time scales, the spectral densities may be decomposed into additive and independent contributions from each of them,^{5,22,34} i.e.

$$j_k = j_{kf} + j_{ks} \quad (12)$$

The orientational dependence of the spectral densities j_k is a consequence of the fact that the efg components $V_k^L(t)$, appearing in the time correlation function in eq 7, refer to a lab-fixed (L) coordinate frame (in which the nuclear spins are quantized). However, the molecular motions—in particular, the diffusion of counterions within the cylindrical aqueous regions—are more conveniently described with reference to a frame fixed in the cylinder (C). Deferring a discussion of the effect of curvature of the cylinder axis, we proceed under the assumption that the C frame coincides with the (local) director frame (D). Trans-

TABLE VII: Reduced Spectral Densities^a

	sample				uncertainty
	I	II	III	IV	
j_f	238	236	208	190	± 15
$j_{lat}(0)$	1178	1213	1598	2113	± 95
$j_{lat}(\omega_0)$	596	476	496	496	± 80
$j_{lat}(2\omega_0)$	260	188	204	196	± 35
$j_{rad}(0)$	45	52	87	102	± 35
$j_{rad}(2\omega_0)$	-83	-117	-82	-62	± 40

^a All spectral densities in units of s^{-1} .

forming the spherical efg tensor components from the L to the D frame, one obtains²²

$$j_k = j_f + F_{k0}(\theta_{LD}) j_{rad}(k\omega_0) + F_{k2}(\theta_{LD}) j_{lat}(k\omega_0) \quad (13)$$

The orientational factors may be expressed in terms of reduced second-rank Wigner rotation matrix elements as

$$F_{km}(\theta_{LD}) = (1/2)\{[d_{km}^2(\theta_{LD})]^2 + [d_{k-m}^2(\theta_{LD})]^2\} \quad (14)$$

Explicit formal expressions for the “reduced” spectral densities $j_{rad}(\omega)$ and $j_{lat}(\omega)$ can be found in ref 22. At this stage, it suffices to note that j_{rad} is associated with radial counterion diffusion, while j_{lat} mainly reflects lateral counterion diffusion around the cylinder axis.

In writing eq 13, we have introduced two simplifications in the fast-motion contribution j_f . First we have assumed that j_f is orientation independent (as indicated by omitting the index k). This is an excellent approximation if the orientational restriction imposed by the interface on the fast motion is weak. That this is actually the case in the present system follows from the smallness of the residual qcc, $\bar{\chi} \approx 150$ kHz (Table IV), as compared to the root-mean-square qcc, $\langle \chi^2 \rangle^{1/2} \gtrsim 4$ MHz.³² Second, we have assumed that j_f is frequency independent in the range 0 – $2\omega_0$. This is certainly the case since the fast-motion time scale³² is much shorter than $1/(2\omega_0) \approx 3 \times 10^{-9}$ s.

Using the explicit expressions for the rotation matrix elements,³⁷ we obtain from eqs 13 and 14, with $\theta_{LD} = 0^\circ$

$$j_0(0^\circ) = j_f + j_{rad}(0) \quad (15a)$$

$$j_1(0^\circ) = j_f \quad (15b)$$

$$j_2(0^\circ) = j_f + \frac{1}{2}j_{lat}(2\omega_0) \quad (15c)$$

and, with $\theta_{LD} = 90^\circ$

$$j_0(90^\circ) = j_f + \frac{1}{4}j_{rad}(0) + \frac{3}{8}j_{lat}(0) \quad (16a)$$

$$j_1(90^\circ) = j_f + \frac{1}{4}j_{lat}(\omega_0) \quad (16b)$$

$$j_2(90^\circ) = j_f + \frac{3}{8}j_{rad}(2\omega_0) + \frac{1}{16}j_{lat}(2\omega_0) \quad (16c)$$

It is seen that the spectral densities at $\theta_{LD} = 90^\circ$ carry the most information about counterion diffusion. In particular, the “lateral” spectral density is probed at three frequencies by the $\theta_{LD} = 90^\circ$ relaxation data (recorded at a single magnetic field).

Equations 15 and 16 constitute a system of six linear equations involving six unknown reduced spectral densities. Substituting the orientation-dependent spectral densities from Table VI, we can thus solve for all the reduced spectral densities. The results, collected in Table VII, will now be discussed in detail, starting with the lateral spectral density $j_{lat}(\omega)$.

Counterion Surface Diffusion. With a slight modification of the treatment in ref 22, the lateral spectral density function may be expressed as

$$j_{lat}(\omega) = (3\pi^2/4)\langle [\bar{\chi}(\mathbf{r})]^2 \rangle \int_0^\infty dt \cos(\omega t) \bar{g}_{lat}(t) \quad (17)$$

(35) Engström, S.; Jönsson, B.; Impey, R. W. *J. Chem. Phys.* **1984**, *80*, 5481.

(36) Schnitker, J.; Geiger, A. *Z. Phys. Chem. (Munich)* **1987**, *155*, 29.

(37) Brink, D. M.; Satchler, G. R. *Angular Momentum*, 2nd ed.; Clarendon Press: Oxford, U.K., 1968.

TABLE VIII: Parameters Derived from Reduced Spectral Densities

	sample			
	I	II	III	IV
$\bar{\chi}_{\text{rms}}^a/\text{kHz}$	194	177	188	197
$\tau_{\text{lat}}^b/\text{ns}$	5.8	7.4	8.8	10.6
$E_f^c/\text{kJ mol}^{-1}$	26.6			24.3

^a Calculated from the fitted $P\bar{\chi}_{\text{rms}}$ parameter, using P values from Table IV. Standard deviation from fit: 2–5 kHz. ^b Standard deviation from fit: 0.2–0.6 ns. ^c Activation energy for j_f from Arrhenius fit. Standard deviation: 2.0 kJ mol⁻¹.

where $\bar{\chi}(\mathbf{r})$ is the counterion qcc locally averaged by fast motions in the neighborhood of the point \mathbf{r} and the angular brackets signify a “coarse-grained” spatial average (over different local environments). The reduced correlation function in eq 17 takes the form

$$\bar{g}_{\text{lat}}(t) = \frac{\langle \bar{\chi}[\mathbf{r}(0)] \bar{\chi}[\mathbf{r}(t)] \cos [2\Delta\phi(t)] \rangle}{\langle [\bar{\chi}(\mathbf{r})]^2 \rangle} \quad (18)$$

where $\Delta\phi(t)$ is the azimuthal (around the cylinder axis) net angular displacement of the counterion during a time t .

As argued above, the locally averaged qcc $\bar{\chi}(\mathbf{r})$ is expected to be significantly different from zero only in a small region near the cylindrical interface. Consequently, we write

$$\langle [\bar{\chi}(\mathbf{r})]^2 \rangle = (P\bar{\chi}_{\text{rms}})^2 \quad (19)$$

where, as before, P is the fraction of counterions in this interfacial region, while $\bar{\chi}_{\text{rms}}$ is the square root of the spatial average of $[\bar{\chi}(\mathbf{r})]^2$ over the interfacial region. The quantity $\bar{\chi}_{\text{rms}}$ is closely related to, but not identical with, the residual qcc $\bar{\chi}$, introduced in eq 5 in connection with the quadrupole splitting. The appearance in eq 19 of P^2 , rather than P , is a consequence of the fact that radial spatial averaging (between the interfacial region and the core) is much faster than lateral (angular) averaging, i.e., $\tau_{\text{rad}} \ll \tau_{\text{lat}}$ (cf. Appendix D and Table VIII).

We also recall that, on account of electrostatic interactions and entropy (cf. Appendix B), nearly all of the counterions are confined to the interfacial region (e.g., $P \approx 0.85$ for $\delta = 5$ Å). As a result, the time correlation function in eq 18 is largely determined by diffusional events taking place within this region; i.e., it essentially reflects counterion diffusion along the curved interface. In this surface diffusion approximation (SDA), eq 18 reduces to

$$\bar{g}_{\text{lat}}(t) = \exp(-t/\tau_{\text{lat}}) \quad (20)$$

with a lateral correlation time

$$\tau_{\text{lat}} = R_e^2/4D \quad (21)$$

Here D is the lateral self-diffusion coefficient of Na⁺ in the interfacial region and R_e is an effective radius for the surface diffusion. In terms of the structural radius R of the aqueous cylinder, we write formally

$$R_e = R - c \quad (22)$$

Combination of eqs 17–20 yields the Lorentzian spectral density function

$$j_{\text{lat}}(\omega) = \frac{3\pi^2}{4} (P\bar{\chi}_{\text{rms}})^2 \frac{\tau_{\text{lat}}}{1 + (\omega\tau_{\text{lat}})^2} \quad (23)$$

The accuracy of the SDA, which led to this simple result, could be assessed by numerical calculations along the lines of ref 22. However, since the SDA was shown²² to be a good approximation for the normal cylindrical geometry (with the counterions outside the cylinder), it is expected to be highly accurate for the reversed cylindrical geometry in the F phase. We thus proceed to fit the two parameters $P\bar{\chi}_{\text{rms}}$ and τ_{lat} in eq 23 to the $j_{\text{lat}}(\omega)$ data in Table VII. The experimental data are clearly compatible with a Lorentzian dispersion, as illustrated in Figure 5 for samples I and IV.

The parameters obtained from the fits are given in Table VIII, with the rms residual qcc calculated by using P values from Table

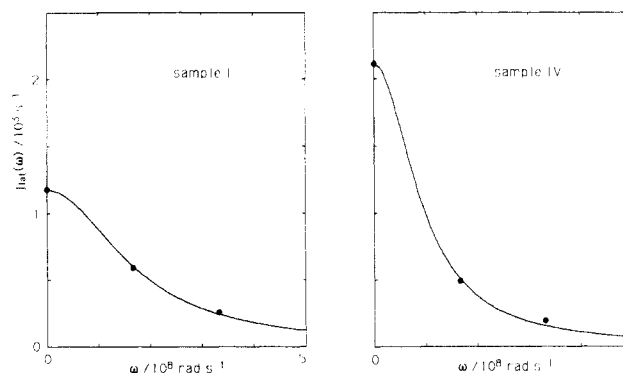


Figure 5. Fits of the spectral density function, eq 23, for counterion surface diffusion to the experimentally determined $j_{\text{lat}}(\omega)$ data for samples I and IV.

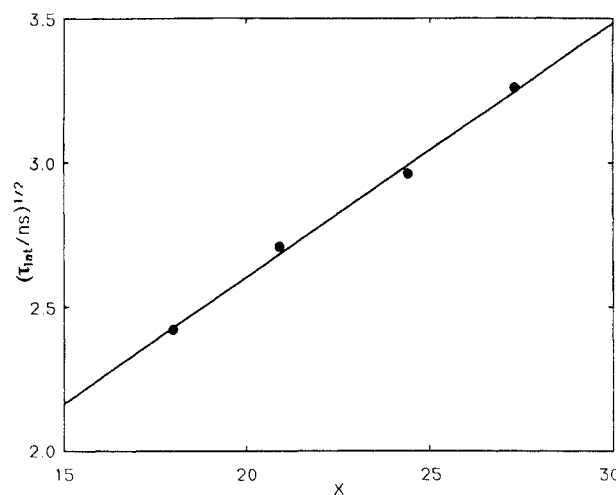


Figure 6. Linear dependence of the square root of the lateral correlation time on the D₂O/AOT mole ratio, x .

IV. The similarity between the $\bar{\chi}_{\text{rms}}$ values and the $\bar{\chi}$ values deduced from the quadrupolar splittings (Table IV) is reassuring. The relatively small difference between the two kinds of residual qcc is in the expected direction. Since, in $\bar{\chi}_{\text{rms}}$, but not in $\bar{\chi}$, $\bar{\chi}(\mathbf{r})$ is squared before it is spatially averaged within the interfacial region (cf. eqs 5 and 19), it follows that $\bar{\chi}_{\text{rms}} \geq \bar{\chi}$.

Turning our attention to the correlation time τ_{lat} , we combine eqs 1b, 21, and 22 to obtain

$$\tau_{\text{lat}}^{1/2} = \frac{v_w^0}{a_s^0 D^{1/2}} x + \frac{1}{2D^{1/2}} (R'_s - c) \quad (24)$$

Like eq 1b, this relation is valid only for $x > x_0 \approx 15$. To ensure that this inequality is satisfied, we have restricted the present study to samples with relatively high water content ($x = 18.0$ – 27.3). By so doing, we avoid the problematic issue of assigning numerical values to the model-dependent quantities R'_s and c . By plotting the square root of the correlation time versus the D₂O/AOT molar ratio x (known from the composition of the samples; cf. Table I), we should obtain a straight line, the slope of which yields the Na⁺ surface diffusion coefficient D . It should be noted that, to deduce D , we do not need to know the actual cylinder radius, nor do we need to estimate the distance parameter c . Moreover, if the AOT preparation used to make up the F-phase samples contains a small amount of water, this merely alters the intercept without affecting the slope in the $\tau_{\text{lat}}^{1/2}$ versus x plot. All that is needed to determine D is the volume per molecule in bulk D₂O, $v_w^0 = 30$ Å³, and the large- x limit of the AOT headgroup area, $a_s^0 = 65$ Å², as determined by X-ray studies of the F phase.¹⁵

As seen from Figure 6, the linear relationship is indeed obeyed. The resulting diffusion coefficient is $D = (2.75 \pm 0.3) \times 10^{-10}$ m² s⁻¹, which is a factor of 3.6 smaller than the diffusion coefficient, $D_0 = 0.98 \times 10^{-9}$ m² s⁻¹, of Na⁺ in an infinitely dilute aqueous (D₂O) electrolyte solution at 20.6 °C. The complexity

of the interfacial region prevents us from giving a simple molecular interpretation of the experimentally determined Na^+ diffusion coefficient. (Even in the case of bulk electrolyte solutions, ionic self-diffusion at high concentrations is not well-understood.³⁸) The principal factors responsible for the reduction of D are direct interactions—repulsive (e.g., hard core) as well as attractive (e.g., Coulombic)—and hydrodynamic interaction (or its microscopic analogue). Taking $\delta = 5 \text{ \AA}$ and $P = 0.85$ (cf. Table IV), we estimate a mean counterion concentration of about 5 mol dm^{-3} in the interfacial region. For a bulk aqueous NaCl solution at this concentration, $D_0/D = 1.6$.^{39,40} Due to the anisotropy of the interfacial region and the limited mobility of the (headgroup) anions in our system, the comparison with a bulk electrolyte solution is not straightforward. Nevertheless, the comparison suggests that ion pairing is not much more important at the interface than it is in a bulk electrolyte solution of comparable concentration.

Other Slow Motions. As noted above, other slow motions, besides the surface diffusion of counterions around the rod axis, may contribute to the spectral densities in eq 13. We thus expect a contribution from modulation of the locally averaged qcc $\bar{\chi}(r)$ by radial counterion diffusion in and out of the interfacial region. In Appendix D, we estimate that $j_{\text{rad}}(0) \approx 6 \text{ s}^{-1}$ for sample IV, which is well 2 orders of magnitude less than $j_{\text{lat}}(0)$. The experimentally determined $j_{\text{rad}}(0)$ is an order of magnitude larger than this estimate, but the relative experimental uncertainty in this quantity is rather large (Table VII).

The negative values obtained for $j_{\text{rad}}(2\omega_0)$ are, of course, unphysical. The question is only whether they result from a systematic error in the measurements or if they are artifacts generated by the approximations invoked for the derivation of eqs 15 and 16. According to these equations, we should have $j_2(90^\circ) > j_1(0^\circ)$. It is the violation of this inequality by the experimental data (Table VI) that gives rise to a negative $j_{\text{rad}}(2\omega_0)$. Since $j_{\text{rad}}(2\omega_0)$ is determined from $j_2(90^\circ)$, which is obtained from $R_{1s}(\theta_{\text{LD}}=90^\circ)$, the unphysical result may be a consequence of a systematic error in the satellite inversion recovery experiment in the $\theta_{\text{LD}} = 90^\circ$ configuration. Fortunately, none of the other five reduced spectral densities would be affected by an error in $j_2(90^\circ)$.

The alternative possibility, that the negative $j_{\text{rad}}(2\omega_0)$ is caused by a defect in the theory, is potentially more serious, as this defect might also affect the other reduced spectral densities. The only approximation that is likely to play a role here is the neglect of relaxation effects due to spatial variations in the local cylinder orientation with respect to the director. In Appendix E we show that the effect of removing this restriction is 2-fold. First, there appears a direct contribution $j_{\text{cyl}}(0)$ to the zero-frequency spectral density from modulation of θ_{DC} by counterion migration. Second, the orientational factors $F_{km}(\theta_{\text{LD}})$ in eq 13 should be orientationally averaged, thus slightly altering the numerical coefficients in eqs 15 and 16. Since the migration of counterions between differently oriented cylinders is expected to be a very slow process, even a small orientational spread σ_{DC} could produce a significant contribution to the zero-frequency spectral density. (Note that this orientational spread is distinct from the static, nonaveraged, orientational spread that gives rise to an asymmetric satellite line shape.)

According to eq E9, the difference $j_0(0^\circ) - j_1(0^\circ)$ furnishes an upper limit for $j_{\text{cyl}}(0)$. The largest value occurs for sample IV, for which we obtain $j_{\text{cyl}}(0) < 100 \text{ s}^{-1}$. On physical grounds, we expect that the correlation time τ_{cyl} for θ_{DC} modulation is much longer than τ_{lat} , probably in the microsecond range at least. With the aid of eq E11, we can then infer that the motionally averaged orientational spread σ_{DC} is less than $5\text{--}10^\circ$. While it is possible that the quantity $j_{\text{rad}}(0)$ in Table VII is due, at least partly, to a partial averaging of the orientational disorder, this probably cannot explain the observation that $j_1(0^\circ) > j_2(90^\circ)$, which would

require $\sigma_{\text{DC}} > 15^\circ$. The most important conclusion, however, is that σ_{DC} is so small that the numerical coefficients in eqs 15 and 16 are only marginally affected. In particular, explicit calculations demonstrate that the deduced lateral correlation time τ_{lat} is virtually unchanged for any reasonable amount of orientational disorder. In fact, even if we postulate that there are no contributions from other slow motions, i.e., if we set $j_{\text{rad}}(0) = j_{\text{rad}}(2\omega_0) = 0$ in eqs 15 and 16, the resulting τ_{lat} values differ from those in Table VIII by only 1–2%, whereas j_f then becomes frequency dependent.

Fast Local Motions. The contribution to the spectral densities from the fast motions may be expressed as²²

$$j_f = (\pi^2/5)[P\langle\chi^2\rangle\tau_f + (1-P)\langle\chi^2\rangle^0\tau_f^0] \quad (25)$$

where $\langle\chi^2\rangle$ is the mean-square qcc, τ_f is an effective correlation time for the local motions, and a superscript zero refers to the supposed bulklike region away from the interface ($0 < r < R - \delta$). As seen from eq 15b, j_f is obtained directly from $j_1(0^\circ)$ and is thus rather accurately determined. In a dilute bulk aqueous (D_2O) NaCl solution,³³ the relaxation rate $R = (2\pi^2/5)\langle\chi^2\rangle^0\tau_f^0$ is about 20 s^{-1} , whence the contribution (ca. 1 s^{-1}) from the second term in eq 25 is completely negligible. With $P = 0.85$ and j_f values from Table VII, we thus calculate that the ratio $\langle\chi^2\rangle\tau_f/\langle\chi^2\rangle^0\tau_f^0$ is in the range 22–28 for our samples. For comparison, in aqueous solutions of simple sodium salts at 5 mol dm^{-3} (corresponding to the mean counterion concentration in the interfacial region), this ratio is merely 1.5–4,³³ whereas in dilute DNA solutions,⁸ it is 5.

Since the quantities $\langle\chi^2\rangle$ and τ_f are determined by a variety of local interactions and dynamics in the interfacial region, it would be unwise to attempt a detailed interpretation. In particular, continuum-solvent models fail spectacularly in accounting for $\langle\chi^2\rangle$.³² Nevertheless, certain conclusions may be drawn without invoking detailed models. A recent molecular dynamics simulation study³² of a model system that is similar to the present one indicates that $\langle\chi^2\rangle$, which is determined mainly by fluctuations in the primary solvation shell of the counterion, is not much different from $\langle\chi^2\rangle^0$. However, a small fraction of the fluctuation amplitude is associated with localized relative motions of counterions and AOT sulfonate headgroups. As these motions are expected to be 1 or 2 orders of magnitude slower than the hydration shell fluctuations (but still faster than $1/\omega_0$, whence the frequency independence of j_f), they probably account for the major part of $\langle\chi^2\rangle\tau_f$. Hence, in the F phase, j_f may have an entirely different physical origin than in a dilute electrolyte solution. This conclusion may have an important bearing on recent attempts at theoretical modeling of counterion spin relaxation in heterogeneous solution systems.⁴¹ In the case of DNA solutions, the increase of j_f (by a factor of 5) from the bulk value was correlated with the slowing down of water reorientation at the interface.⁸ At the AOT/water interface, however, the increase of j_f (by a factor of 22–28) is an order of magnitude larger than the slowing down of interfacial water reorientation (a factor of 3), as recently determined by ^2H and ^{17}O spin relaxation in the L_2 phase of the AOT/ D_2O /isooctane system.²⁸

The effect of temperature was studied for samples I and IV within the relatively narrow stability range of the F phase. This study was limited to measurements of R_{1s} and R_c^{hom} in the $\theta_{\text{LD}} = 0^\circ$ configuration. As shown above, these relaxation rates suffice to determine $j_f = R_c^{\text{hom}}(0^\circ) - R_{1s}(0^\circ)/2$ and $j_{\text{lat}}(2\omega_0) = 2[R_{1s}(0^\circ) - R_c^{\text{hom}}(0^\circ)]$. The results are given in Table IX. As shown in Figure 7, the temperature dependence of j_f within the range 12–25 $^\circ\text{C}$ is of the Arrhenius type. The apparent activation energy deduced from the slope is about 25 kJ mol^{-1} (Table VII), which is substantially larger than the activation energy of 12 kJ mol^{-1} for $\langle\chi^2\rangle^0\tau_f^0$ in a dilute NaCl solution.⁸ In view of the different origins of the quadrupolar relaxation in the two cases (cf. above), a different temperature dependence is not unexpected. The activation energy found for j_f is in the range expected for diffusive

(38) Wolynes, P. G. *Annu. Rev. Phys. Chem.* **1980**, *31*, 345.

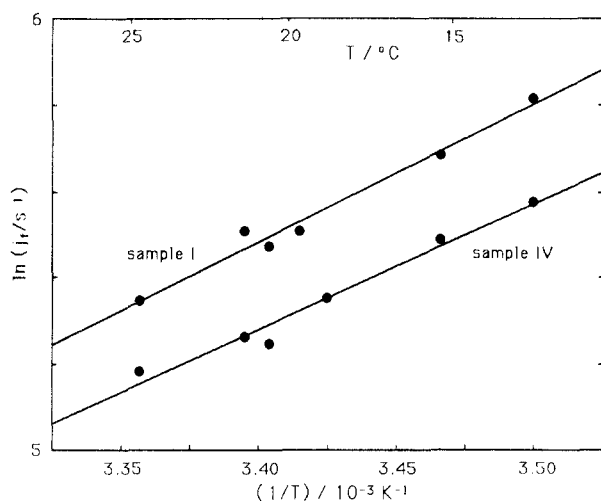
(39) Harris, K. R.; Hertz, H. G.; Mills, R. *J. Chim. Phys.* **1978**, *75*, 391.

(40) Mills, R.; Lobo, V. M. M. *Self-diffusion in Electrolyte Solutions*; Elsevier: Amsterdam, 1989.

(41) Reddy, M. R.; Rossky, P. J.; Murthy, C. S. *J. Phys. Chem.* **1987**, *91*, 4923.

TABLE IX: Temperature Dependence of Quadrupolar Splittings, Relaxation Rates, and Spectral Densities

$T/^{\circ}\text{C}$	$\nu_Q(0^{\circ})/\text{kHz}$	$R_{1s}(0^{\circ})/\text{s}^{-1}$	$R_c^{\text{hom}}(0^{\circ})/\text{s}^{-1}$	j_t/s^{-1}	$j_{\text{lat}}(2\omega_0)/\text{s}^{-1}$
Sample I					
12.6	32.81	880	776	336	207
15.4	32.86	832	710	294	245
19.7	32.96	757	625	247	264
20.6	33.05	735	606	238	260
21.4	32.98	713	603	247	220
24.7	33.08	672	547	210	251
uncertainty	± 0.05	± 20	± 10	± 15	± 35
Sample IV					
12.6	28.56	666	597	264	138
15.4	28.71	622	553	242	138
18.8	28.89	578	500	211	156
20.6	28.93	575	478	190	196
21.4	28.96	550	468	193	164
24.7	29.08	512	434	178	156
uncertainty	± 0.05	± 20	± 10	± 15	± 35

**Figure 7.** Temperature dependence of the spectral density j_t due to fast local motions, for samples I and IV.

processes (as opposed to librations and intermolecular vibrations, which do not involve disruption of hydrogen bonds) in aqueous media (cf. below).

The temperature dependence of $j_{\text{lat}}(2\omega_0)$ is weak (in fact, barely significant), as expected in the dispersive region of the Lorentzian spectral density in eq 23. The maximum in $j_{\text{lat}}(2\omega_0)$ should occur at the temperature where $\tau_{\text{lat}} = 1/(2\omega_0)$, and our data are approaching this maximum from the low-temperature side. Due to the weak temperature dependence, we cannot accurately determine the activation energy for τ_{lat} , but the data are consistent with an activation energy in the range 10–30 kJ mol⁻¹. (In NaCl solutions up to 5 mol dm⁻³, the Na⁺ diffusion coefficient^{39,40} has an activation energy of 18–20 kJ mol⁻¹.)

Concluding Discussion

The present study demonstrates that counterion spin relaxation is a powerful method for elucidating structure and dynamics in anisotropic systems. In contrast to the case of isotropic systems, all the spectral densities can be determined from measurements at a single magnetic field. Furthermore, by exploiting the orientational dependence of the spectral densities, contributions from motional modes with different symmetry properties can be separated. Thanks to these fortunate circumstances, the interpretation of the relaxation data becomes considerably less model dependent than for isotropic heterogeneous systems.

In the course of this study, we have obtained valuable insights about the structure of the F phase and about the fast local motions in the interfacial region. More importantly, however, we have determined the diffusion coefficient of sodium ions in the interfacial region. To the best of our knowledge, this is the first

determination of a local counterion diffusion coefficient in any heterogeneous aqueous system.

The counterion diffusion coefficient in the F phase could, in principle, be determined also by the field-gradient spin-echo (FGSE) NMR technique.⁴² Unfortunately, signal-to-noise considerations limit the FGSE method to nuclei (such as ⁷Li⁺) with relatively long relaxation times. Even then, it may be difficult to deduce the local diffusion coefficient, since the FGSE method yields a macroscopic diffusion coefficient (deduced from root-mean-square displacements of the order 10⁻⁶ m), which may be strongly affected by diffusional barriers associated with large-scale sample inhomogeneities (such as domain boundaries). Even if this potential complication could be avoided, the diffusion coefficient obtained from a FGSE experiment would differ from that determined here in two respects. First, the FGSE experiment measures diffusion along the aqueous rod axis, whereas the ²³Na relaxation experiment reported here probes diffusion around the rod axis. However, since the counterion diffusion coefficient is expected to be determined mainly by local interactions, the difference in interfacial curvature in the two cases should be of minor importance. Second, and more importantly, the radial averaging of the local diffusion coefficient is qualitatively different in the two experiments. In the FGSE experiment, the relatively few counterions that reside in the bulklike central core region are more heavily weighted than the less mobile counterions in the interfacial region. The radial counterion distribution must therefore be accurately known in order to deduce a surface diffusion coefficient. This becomes a serious problem if the surface mobility is much lower than the bulk mobility. In our ²³Na relaxation experiment, on the other hand, the counterion mobility is weighted by the locally averaged qcc $\bar{\chi}(\mathbf{r})$, which is essentially zero except within the interfacial region. Hence, the experimentally determined diffusion coefficient is, to an excellent approximation, a surface diffusion coefficient.

As far as we know, only one FGSE study of counterion diffusion in a lyotropic mesophase has been reported in the literature, namely, a ⁷Li study of the perfluorooctanoate/water system.⁴³ As the structures of the investigated mesophases in this system are complex,⁴⁴ it is not straightforward to deduce a local diffusion coefficient. Nevertheless, a simplified analysis⁴⁴ suggests that the large observed Li⁺ mobility reduction—a factor of 50 relative to a dilute aqueous LiCl solution—is due mainly to local interactions (rather than to global obstruction effects). The much larger mobility reduction in the lithium perfluorooctanoate system, as compared to our system, is surely related to the lower water content ($x = 9$) but may also reflect a stronger ion-pairing tendency.

Molecular dynamics (MD) computer simulation may also be used to study counterion surface diffusion.⁴⁵ While this approach can, in principle, provide a much more detailed picture than any experimental technique, present-day interaction potentials have probably not yet reached the stage of refinement where quantitatively accurate results can be expected. Furthermore, since very large systems (in terms of the number of interaction sites) must be simulated, only short time scales are accessible. For example, in the recent MD study by Linse,⁴⁵ Na⁺ diffusion coefficients were calculated from root-mean-square displacements of about 2 Å, where the ion may still be trapped in a local potential well or “correlation hole”. In contrast, our diffusion coefficient was derived from correlation times of the order 10⁻⁸ s, corresponding to a root-mean-square displacement in excess of 20 Å. On this length scale, all local surface inhomogeneities have been thoroughly averaged.

A knowledge of the diffusion coefficient of ions at interfaces is important in a variety of problems in colloid and polymer science, electrochemistry, and biophysics. As an example, the macroscopic counterion diffusion coefficients measured in polyelectrolyte solutions^{46–48} are often considerably smaller than predicted by

(42) Stilbs, P. *Prog. NMR Spectrosc.* **1987**, *19*, 1.

(43) Tiddy, G. J. T. *J. Chem. Soc., Faraday Trans. 1* **1977**, *73*, 1731.

(44) Kekicheff, P.; Tiddy, G. J. T. *J. Phys. Chem.* **1989**, *93*, 2520.

(45) Linse, P. *J. Chem. Phys.* **1989**, *90*, 4992.

theory,⁴⁹ when one assumes that the local counterion diffusion coefficient is the same at the surface of the polyion as in the bulk of the solution. It has been suggested⁴⁶⁻⁴⁸ that this discrepancy may be due to a reduction of the surface diffusion coefficient. This is clearly in line with the results of the present study. On the other hand, our results do not support the assumption of a vanishing surface diffusion coefficient, made in Manning's theory of counterion diffusion.⁵⁰

The counterion spin relaxation behavior in polyelectrolyte solutions should also be affected by surface diffusion, at least if the polyion radius is of the order of 10 Å or more.²² For synthetic polyelectrolytes with thin backbones, such effects are not prominent,⁵ whereas for DNA, the frequency-dependent part of the relaxation rate appears to be dominated by surface diffusion around the helix axis.⁸

Acknowledgment. This work was supported by grants and fellowships from the Swedish Natural Science Research Council. T.C.W. thanks the University of Missouri for granting a research leave and the Research Corporation for partial support.

Appendix A

Satellite Line Shape in the Presence of Sample Inhomogeneity. In this appendix we show how the satellite line shape in a conventional (single $\pi/2$ pulse) spectrum is affected by nonaveraged sample inhomogeneities, i.e., by a distribution of local director orientations θ_{LD} around a mean director orientation $\bar{\theta}_{LD}$ and by a distribution of motionally averaged quadrupole coupling constants $\langle \chi \rangle_D$.

For a given local director orientation θ_{LD} and a given static residual qcc $\langle \chi \rangle_D$, the $|I k - 1/2\rangle \leftrightarrow |I k + 1/2\rangle$ transition gives rise to a Lorentzian line

$$L_k(\omega; \Delta, \theta_{LD}) = \frac{1}{\pi} \frac{R_k(\theta_{LD})}{[R_k(\theta_{LD})]^2 + [\omega - \omega_Q^k(\Delta, \theta_{LD})]^2} \quad (A1)$$

If the major principal component of the motionally averaged electric field gradient tensor is along an axis with at least 3-fold rotational symmetry (as in the F phase and in most other lyotropic mesophases), then the quadrupolar frequency is given by

$$\omega_Q^k(\Delta, \theta_{LD}) = k\Delta P_2(\theta_{LD}) \quad (A2)$$

where $P_2(\theta_{LD}) = (3 \cos^2 \theta_{LD} - 1)/2$ and

$$\Delta = 2\pi \frac{3\langle \chi \rangle_D}{2I(2I - 1)} \quad (A3)$$

We consider first the effect of a distribution of $\langle \chi \rangle_D$ values. For simplicity, we assume a rectangular distribution

$$g(\Delta) = \begin{cases} \frac{1}{2\delta}, & |\Delta - \Delta_0| \leq \delta \\ 0, & \text{otherwise} \end{cases} \quad (A4)$$

The Δ -averaged line shape then becomes

$$\begin{aligned} \langle L_k(\omega; \theta_{LD}) \rangle_\Delta &= \int d\Delta g(\Delta) L_k(\omega; \Delta, \theta_{LD}) \\ &= \frac{1}{\pi R_k(\theta_{LD})} \frac{\arctan[(1-x+\epsilon)\Lambda] - \arctan[(1-x-\epsilon)\Lambda]}{2\epsilon\Lambda} \end{aligned} \quad (A5)$$

where $\epsilon = \delta/\Delta_0$ is the relative spread in the qcc, $x = \omega/\omega_Q^k(\Delta_0, \theta_{LD})$ is the reduced frequency, and $\Lambda = \omega_Q^k(\Delta_0, \theta_{LD})/R_k(\theta_{LD})$ is the splitting-to-line width ratio. In the limit $\epsilon = 0$, eq A5 reduces to eq A1 with $\Delta = \Delta_0$. It follows from eq A5 that the line shape is symmetric around $\omega = \omega_Q^k(\Delta_0, \theta_{LD})$ and that the half-width at

half-amplitude is (in angular frequency units) $(1 + \epsilon^2\Lambda^2)^{1/2}R_k(\theta_{LD})$. Further, it can be shown that the deviation from Lorentzian line shape is small if $\epsilon\Lambda < 1$. We then have, as a good approximation

$$\langle L_k(\omega; \theta_{LD}) \rangle_\Delta = \frac{1}{\pi} \frac{(1 + \epsilon^2\Lambda^2)^{1/2}R_k(\theta_{LD})}{(1 + \epsilon^2\Lambda^2)[R_k(\theta_{LD})]^2 + [\omega - \omega_Q^k(\Delta_0, \theta_{LD})]^2} \quad (A6)$$

The effect of a distribution $f(\theta_{LD})$ of local director orientations around a mean value $\bar{\theta}_{LD}$ is to produce the superposition spectrum

$$\langle L_k(\omega) \rangle_{\Delta, \theta_{LD}} = \int d\theta_{LD} f(\theta_{LD}) \langle L_k(\omega; \theta_{LD}) \rangle_\Delta \quad (A7)$$

The θ_{LD} dependence in $\langle L_k(\omega; \theta_{LD}) \rangle_\Delta$ comes essentially from the term $[\omega - \omega_Q^k(\Delta_0, \theta_{LD})]^2$ in eq A6. Hence, we may evaluate R_k and Λ at $\theta_{LD} = \bar{\theta}_{LD}$. Further, we assume that $f(\theta_{LD})$ has a Gaussian form, i.e.

$$f(\theta_{LD}) = C \exp\left[-\frac{(\theta_{LD} - \bar{\theta}_{LD})^2}{2\sigma^2}\right] \quad (A8)$$

where C is a normalization constant and $\sigma = \langle (\theta_{LD} - \bar{\theta}_{LD})^2 \rangle^{1/2}$ is the rms deviation around the mean. Combination of eqs A6–A8 then yields, after a numerical integration, the inhomogeneous satellite line shape for given values of the splitting Δ_0 , the homogeneous line width $R_k(\bar{\theta}_{LD})$, and the inhomogeneity parameters ϵ and σ . In contrast to the qcc spread, the θ_{LD} spread not only causes line broadening but also induces a line shape asymmetry and a shift of the satellite peak.

Appendix B

Counterion Distribution in a Cylindrical Region. Here we derive an expression for the fraction of counterions residing within a distance δ of the charged interface in a cylindrical aqueous region of radius R . We describe the interactions in a primitive model, where the counterions are treated as point charges embedded in a dielectric continuum of relative permittivity ϵ_r , bounded by a cylindrical interface carrying a uniform surface charge density $\sigma = -e/a_s$, where a_s is the surfactant headgroup area. In a mean-field approximation (neglecting the correlations among the counterions), the local counterion density is determined by the mean electrostatic potential $\Psi(r)$, which is obtained by solving the Poisson–Boltzmann equation

$$\frac{1}{r} \frac{d}{dr} \left[r \frac{d\Psi(r)}{dr} \right] = -\frac{zen(0)}{\epsilon_0\epsilon_r} \exp\left[-\frac{ze\Psi(r)}{k_B T}\right] \quad (B1)$$

where z is the counterion valency and $n(0)$ is the counterion density at the center of the cylindrical region. The boundary conditions follow from symmetry

$$\left. \frac{d\Psi}{dr} \right|_{r=0} = 0 \quad (B2)$$

and from Gauss' law

$$\left. \frac{d\Psi}{dr} \right|_{r=R} = \frac{\sigma}{\epsilon_0\epsilon_r} \quad (B3)$$

The reversed cylindrical geometry is remarkable in that it is the only case for which there exists an exact closed-form analytical solution to the Poisson–Boltzmann equation. (The planar and normal cylindrical geometries also admit analytical solutions, which, however, involve a coupling constant that can be calculated from the system parameters only by numerically solving a transcendental equation.) For the electric field, one obtains^{51,52}

$$E(r) = -\frac{d\Psi}{dr} = \frac{k_B T}{ze} \frac{4r}{(1 + 1/\Gamma)R^2 - r^2} \quad (B4)$$

with the dimensionless coupling parameter

(46) Nilsson, L. G.; Nordenskiöld, L.; Stilbs, P.; Braunlin, W. H. *J. Phys. Chem.* **1985**, *89*, 3385.

(47) Rymdén, R.; Stilbs, P. *J. Phys. Chem.* **1985**, *89*, 2425.

(48) Piculell, L.; Rymdén, R. *Macromolecules* **1989**, *22*, 2376.

(49) Yoshida, N. *J. Chem. Phys.* **1978**, *69*, 4867.

(50) Manning, G. S. *J. Chem. Phys.* **1969**, *51*, 934.

(51) Jönsson, B. Thesis, University of Genarp, Sweden, 1981.

(52) Lampert, M. A.; Martinelli, R. U. *Chem. Phys.* **1984**, *88*, 399.

$$\Gamma = \frac{|ze\sigma|R}{4\epsilon_0\epsilon_r k_B T} \quad (\text{B5})$$

From Gauss' law it follows that the fraction P of counterions in the interfacial region, $R - \delta < r < R$, is

$$P = 1 + (1 - \lambda) \frac{\epsilon_0 \epsilon_r}{\sigma} E(R - \delta) \quad (\text{B6})$$

with $\lambda = \delta/R$. Combination of eqs B4–B6 now yields the desired result

$$P = \frac{\Gamma + 1}{\Gamma + [\lambda(2 - \lambda)]^{-1}} \quad (\text{B7})$$

Appendix C

Effect of Nonaveraged Orientational Disorder on Relaxation Rates. Here we discuss the static effects on the measured relaxation rates of (i) the nonaligned part of the sample and (ii) the spread of local director orientations θ_{LD} . Since, for a given spread in θ_{LD} , we have $\Delta R \ll \Delta\omega_Q$, it is possible to be in the motional averaging regime with respect to relaxation and in the static regime with respect to the line shape. But since it will prove sufficient to estimate an upper limit for the effect, we may disregard this potential complication.

We consider first the relaxation rates R_c^{hom} and R_c^{QE} , derived from the central line in the ^{23}Na spectrum (in the F2 dimension). This line is associated with the $|3/2 \ 1/2\rangle \leftrightarrow |3/2 \ -1/2\rangle$ Zeeman transition, which (to first order) is unaffected by the static quadrupole coupling.²⁹ The shape of the central line is therefore unaffected by orientational disorder. However, if the spectral densities are orientation dependent, then the relaxation rates derived from the central line are affected. The measured relaxation rates R_c^{hom} and R_c^{QE} should therefore be corrected for the fraction f of the central line intensity contributed by the nonaligned part of the sample. Now, from Table V, it is clear that R_c^{hom} has the same value, within the experimental uncertainty, for the two orientations. (This invariance is a numerical coincidence that would not obtain, for example, at a different Larmor frequency. The spectral densities j_1 and j_2 are, in fact, orientation dependent, as seen from Table VI.) Since the nonaligned fraction corresponds either to $\theta_{LD} = 90^\circ$ or to a powder (cf. the section on Static Properties), it follows that the measured R_c^{hom} does not need to be corrected. This conclusion applies also to R_c^{QE} , which is governed by the same linear combination of spectral densities as R_c^{hom} (cf. eqs 9 and 10). The small variation in R_c^{QE} with orientation (Table V) is caused by differences in the magnetic field inhomogeneity broadening in the two configurations.

The θ_{LD} spread within the aligned part of the sample will give rise to a central line composed of a superposition of Lorentzians of different widths but centered on the same frequency. With a θ_{LD} spread of $\sigma = 5^\circ$ (cf. Table III), we calculate, using eqs 9, 13 and 14 and spectral densities from Table VII, that the spread in R_c^{hom} is about 1 s^{-1} . As this is well within the experimental uncertainty, the effect of θ_{LD} spread may safely be neglected.

The relaxation rates R_{1s} and R_s^{QE} are derived from the satellites in the F2 dimension. For samples in the $\bar{\theta}_{LD} = 0^\circ$ configuration, the nonaligned fraction presents no problem, since the satellites from the aligned fraction appear at twice the splitting of the satellites from the nonaligned fraction. For samples in the $\bar{\theta}_{LD} = 90^\circ$ configuration, on the other hand, the satellites from the two fractions overlap. Since the relaxation rates R_{1s} and R_s^{QE} are deduced from the pulse delay time dependence of the satellite peak amplitude, the correction should be based on the fractional peak amplitude f^* contributed by the nonaligned part of the sample, rather than on the actual fraction f of this part (cf. Table I). The fraction f^* , which depends on the θ_{LD} distributions in both parts of the sample, can be estimated from ^{23}Na F2 spectra in the $\bar{\theta}_{LD} = 0^\circ$ configuration, where the satellites from the two parts are distinct. For the four investigated samples, the peak amplitude fraction f^* is about a factor of 3 smaller than the fraction f obtained from the integrated intensities in the ^2H spectrum. The correction is thus rather small. Furthermore, irrespective of

whether the nonaligned part is a 2D or 3D powder (in the $\bar{\theta}_{LD} = 90^\circ$ configuration), the peak amplitude will be dominated by contributions from crystalline domains with orientations in the neighborhood of $\theta_{LD} = 90^\circ$, just as for the aligned part. As a result, the correction that should be applied to the measured rates R_{1s} and R_s^{QE} is well within the experimental uncertainty and can therefore be ignored.

As regards the θ_{LD} spread in the aligned part, the same type of considerations as for the central line yield a spread in the relaxation rates of less than 5 s^{-1} . The effect of this small spread is further reduced by the fact that satellites corresponding to $\theta_{LD} = \bar{\theta}_{LD} \pm \sigma$ are displaced by an amount of the order of the line width and, hence, contribute less to the peak amplitude.

In conclusion, then, we can safely neglect all static effects of orientational disorder on all measured relaxation rates. This conclusion is consistent with the fact that no deviations from exponential inversion recovery or Lorentzian central line shapes in the F1 dimension could be detected.

Appendix D

Spectral Density for Radial Counterion Diffusion. The contribution to the spectral density function from modulation of the locally averaged qcc $\bar{\chi}(\mathbf{r})$ by radial counterion diffusion within the cylindrical aqueous region may be expressed, in analogy with eqs 17 and 18, as²²

$$j_{\text{rad}}(\omega) = \frac{\pi^2}{4} \int_0^\infty dt \cos(\omega t) \langle \bar{\chi}[\mathbf{r}(0)] \bar{\chi}[\mathbf{r}(t)] \rangle \quad (\text{D1})$$

Assuming that the radial motion of the counterions can be described by a mean-field Smoluchowski-type diffusion equation,⁵³ we obtain for the zero-frequency spectral density²²

$$j_{\text{rad}}(0) = \frac{\pi^2}{4} P(1 - P) \bar{\chi}_{\text{rms}}^2 \tau_{\text{rad}} \quad (\text{D2})$$

where $\bar{\chi}_{\text{rms}}$ is the residual qcc locally averaged within the interfacial region, which contains a fraction P of the counterions and has a radial extension δ . Furthermore, the characteristic time τ_{rad} for relaxation of the regional counterion populations is given by^{22,54}

$$\tau_{\text{rad}} = \frac{P}{(1 - P)D_0} \int_0^{R-\delta} \frac{dr}{r f(r)} \left[\int_0^r ds f(s) \right]^2 + \frac{(1 - P)}{PD} \int_{R-\delta}^R \frac{dr}{r f(r)} \left[\int_r^R ds f(s) \right]^2 \quad (\text{D3})$$

where D and D_0 are the counterion diffusion coefficients inside and outside the interfacial region, respectively, and $f(r)$ is the radial counterion distribution

$$f(r) = \exp[-w(r)] / \int_0^R dr r \exp[-w(r)] \quad (\text{D4})$$

with the reduced potential $w(r) = ze\Psi(r)/(k_B T)$.

Using the Poisson–Boltzmann potential (Appendix B), we obtain from eqs D3 and D4

$$\tau_{\text{rad}} = \frac{R^2}{8} (1 - \lambda)^2 \left\{ \frac{\lambda(2 - \lambda)}{D_0} + \frac{1}{D} \left[(1 - \lambda)^2 - 3 - \frac{4 \ln(1 - \lambda)}{\lambda(2 - \lambda)} \right] \right\} \quad (\text{D5})$$

where $\lambda = \delta/R$. This result is remarkable, and peculiar to the reversed cylindrical geometry, in that τ_{rad} is independent of the ionic charge.

With $\delta = 5 \text{ \AA}$, $R = 31.2 \text{ \AA}$ (corresponding to sample IV), $D_0 = 1.2 \times 10^{-9} \text{ m}^2 \text{ s}^{-1}$ (bulk value), and $D = 2.8 \times 10^{-10} \text{ m}^2 \text{ s}^{-1}$ (as determined from j_{lat}), we obtain from eq D5 $\tau_{\text{rad}} = 0.44 \text{ ns}$. With $P = 0.831$ (Table VI) and $\bar{\chi}_{\text{rms}} = 197 \text{ kHz}$ (Table VIII), eq D2 then yields $j_{\text{rad}}(0) = 6 \text{ s}^{-1}$.

(53) Åkesson, T.; Jönsson, B.; Halle, B.; Chan, D. Y. C. *Mol. Phys.* **1986**, *57*, 1105.

(54) Halle, B. *Mol. Phys.* **1985**, *56*, 209.

Appendix E

Relaxation Due to Motional Averaging of Orientational Disorder. If there is a spread in the orientation of the cylindrical aggregates with respect to the director, and if the counterions sample different orientations at a rate that is short compared to the corresponding quadrupolar frequency difference, then there exists a new mechanism for relaxation and eq 13 must be modified accordingly.

Let τ_{DC} be the correlation time for the motion whereby a counterion migrates between distinct nonparallel cylindrical aggregates or diffuses between differently oriented segments of a contiguous cylindrical region. On physical grounds, we expect that τ_{DC} is much longer than τ_{rad} and τ_{lat} . We can then analyze the effect of orientational disorder by a straightforward extension of the treatment in ref 22 to three disjoint time scales. Further, since τ_{lat} is of order $1/\omega_0$, it follows that Ω_{DC} modulation will contribute only to the zero-frequency spectral density $j_0(0; \theta_{LD})$. (Ω_{DC} denotes the set of Euler angles describing the local cylinder orientation with respect to the director.) We thus find that eq 13 should be supplemented with a contribution

$$j_k^{DC} = \delta_{k0} \sum_{m=-2}^2 [d_{0m}^2(\theta_{LD})]^2 j_{cyl}^m(0) \quad (E1)$$

where

$$j_{cyl}^m(0) = \frac{\pi^2}{4} (P\bar{\chi})^2 A_m \tau_m \quad (E2)$$

$$A_m = \langle [d_{m0}^2(\theta_{DC})]^2 \rangle - \delta_{m0} \langle d_{00}^2(\theta_{DC}) \rangle^2 \quad (E3)$$

$$\tau_m = \frac{1}{A_m} \int_0^\infty dt \{ \langle D_{m0}^2 * [\Omega_{DC}(0)] D_{m0}^2 [\Omega_{DC}(t)] \rangle - \delta_{m0} \langle D_{00}^2(\Omega_{DC}) \rangle^2 \} \quad (E4)$$

For a narrow Gaussian θ_{DC} distribution of width σ_{DC} , we find to leading order

$$A_0 = 4A_2 = \frac{9}{2} \sigma_{DC}^4 \quad (E5)$$

For strong-collision models, with a propagator of the form

$$f(\Omega_{DC}, t | \Omega_{DC}^0) = f(\Omega_{DC}) + [\delta(\Omega_{DC} - \Omega_{DC}^0) - f(\Omega_{DC})] h(t) \quad (E6)$$

it follows that the effective correlation times in eq E4 are independent of m , whence we write $\tau_m = \tau_{cyl}$. If the fluctuation in Ω_{DC} is a result of counterion diffusion within a single cylindrical aggregate with a curved axis, characterized by a finite deflection

length,⁵⁵ then one can show⁵ that τ_{cyl} diverges. This simply means that the motional narrowing approximation, inherent in the conventional relaxation theory, is not valid. This kind of orientational disorder will then give rise to static effects as well as relaxation effects, with a correlation time given by the time integral of the correlation function truncated at a time less than $1/\Delta\omega_Q$. Another possibility is that counterions migrate between cylinders of different orientation. The correlation time τ_{cyl} is then at least equal to the mean counterion residence time in an aggregate. (It is longer if adjacent cylinders are orientationally correlated.)

A further effect of orientational disorder is that the orientational factors in eq 13 should be replaced by orientational averages according to

$$F_{km}(\theta_{LD}) \rightarrow \langle F_{km}(\theta_{LC}) \rangle \quad (E7)$$

For a narrow Gaussian distribution of θ_{LC} around θ_{LD} , we have

$$\langle F_{km}(\theta_{LC}) \rangle = F_{km}(\theta_{LD}) + \frac{\sigma_{DC}^2}{2} \left. \frac{d^2 F_{km}}{d\theta_{LC}^2} \right|_{\theta_{LD}} + \frac{\sigma_{DC}^4}{8} \left. \frac{d^4 F_{km}}{d\theta_{LC}^4} \right|_{\theta_{LD}} + \dots \quad (E8)$$

Neglecting the contribution from radial diffusion (cf. Appendix D), we obtain from eqs 13, 14, E1, and E8, for the two director orientations $\theta_{LD} = 0^\circ$ and $\theta_{LD} = 90^\circ$

$$j_0(0^\circ) = j_f + j_{cyl}(0) \quad (E9a)$$

$$j_1(0^\circ) = j_f + \frac{1}{2} \sigma_{DC}^2 j_{lat}(\omega_0) \quad (E9b)$$

$$j_2(0^\circ) = j_f + \frac{1}{2} (1 - \sigma_{DC}^2) j_{lat}(2\omega_0) \quad (E9c)$$

$$j_0(90^\circ) = j_f + \frac{7}{16} j_{cyl}(0) + \frac{3}{8} (1 - 2\sigma_{DC}^2) j_{lat}(0) \quad (E10a)$$

$$j_1(90^\circ) = j_f + \frac{1}{4} j_{lat}(\omega_0) \quad (E10b)$$

$$j_2(90^\circ) = j_f + \frac{1}{16} (1 + 6\sigma_{DC}^2) j_{lat}(2\omega_0) \quad (E10c)$$

where, according to eqs E2 and E5

$$j_{cyl}(0) \equiv j_{cyl}^0(0) = 4j_{cyl}^2(0) = \frac{9\pi^2}{8} (P\bar{\chi})^2 \sigma_{DC}^4 \tau_{cyl} \quad (E11)$$

Registry No. AOT, 577-11-7; Na, 7440-23-5; isooctane, 540-84-1.

(55) Odijk, T. *Macromolecules* **1986**, *19*, 2313.